1-1-2011

Synthesis of TiO2-Based Photocatalyst and Their Environmental Applications

Jinho Park

Follow this and additional works at: https://openscholarship.wustl.edu/etd

WASHINGTON UNIVERSITY IN ST. LOUIS

School of Engineering and Applied Science

Department of Energy, Environmental and Chemical Engineering

Thesis Examination Committee:
Pratim Biswas, Chair
Venkat Subramanian
Yinjie Tang

SYNTHESIS OF TiO_2-BASED PHOTOCATALYST AND

THEIR ENVIRONMENTAL APPLICATIONS

by

Jinho Park

A thesis presented to the School of Engineering
of Washington University in partial fulfillment of the
requirements for the degree of

MASTER OF SCIENCE

August 2011
Saint Louis, Missouri

ABSTRACT OF THE THESIS

Synthesis of TiO_2-Based Photocatalyst and

Their Environmental Applications

by

Jinho Park

Master of Science in Energy, Environmental and Chemical Engineering

Washington University in St. Louis, 2011

Research Advisor: Professor Pratim Biswas

Synthesis TiO_2-based photocatalyst by aerosol routes were investigated. The synthesized photocatalysts were applied for environmental fields: CO_2 photoreduction and photocatalytic inactivation of pathogenic microorganisms in water. As one part of them, nanostructured copper doped titania-silica (Cu-TiO_2-SiO_2) photocatalyst composite particles were directly formed in a rapid manner by evaporation driven self-assembly of nanocolloids in a furnace aerosol reactor (FuAR). Aqueous suspensions of nanosized TiO_2 and SiO_2 colloids and copper nitrate solution were used as precursors. The size, composition, and porosity of the composite particles were tailored by manipulating the precursor concentration, stoichiometric ratio, and synthesis temperature, respectively. The as-prepared composite particles were characterized by means of SEM, TEM, XRD, UV-VIS, and nitrogen physisorption measurements, to determine particle diameter, morphology, crystallinity, absorption band, surface area, and pore size. CO_2 photoreduction was conducted inside a quartz reactor under illumination of UV light followed by GC analysis. The results revealed that the composite particles were

submicrometer-sized mesoporous spheres with average pore sizes of 20 to 30 nm, having optimal molar percentages of TiO_2 and Cu to the whole particle of 2% and 0.01%, respectively, achieving a relatively high CO_2 conversion efficiency, i.e. CO yield of approximately 20 μmol/g-TiO_2/hr. As the second part of the study, TiO_2 nanostructured films were synthesized by aerosol chemical vapor deposition method (ACVD) with different controlled morphologies: columnar, granular and branched structure for the photocatalytic inactivation of *Escherichia coli* (*E. coli*) in water. Effects of film morphology and external applied voltage on inactivation rate were investigated. As-prepared films were characterized using SEM, TEM, XRD and UV-VIS. Photochemical and photoelectrochemical inactivation of *E. coli* in water using as-prepared TiO_2 films were performed under irradiation of UVA light. Inactivation rate constant of each case were obtained from each inactivation curve to compare them. The inactivation rate constant for the columnar film was enhanced 430% by applied voltage on the film while that for the branched film was increased only 130% by the applied bias. Photochemical inactivation rate of the columnar and the branched films were also discussed to figure out effect of surface area which was obtained from estimation.

Acknowledgments

First of all, I would like to give thanks to my Lord God for his complete help for this work. And I wish that God's glory would be praised through my work.

I would like to thank my advisor, Professor Pratim Biswas, Department of Energy, Environmental and Chemical Engineering, Washington University in St. Louis, for his education, guidance, encouragement, support and patient throughout two years of my study.

I would like also to thank Professor Venkat Subramanian and Professor Yinjie Tang, Department of Energy, Environmental and Chemical Engineering, Washington University in St. Louis, for spending their important time for reviewing my dissertation.

A special thanks goes to AAQRL members, Dr. Wei-Ning Wang, Dr. Manoranjan Sahu, Dr. Eric Kettleson, Dr. Anna Leavey, Vivek Shah, Xiaofei Wang, Tandeep Chadha, and Craig Jacobson, for help with experimental work and supporting me. Especially, I would like to thank Mr. Woo-Jin An for his help and valuable guidance during two years in St. Louis.

Finally, I wish to dedicate this work to my parents, sister and my lovely wife, Jiyang Oh, for their love, sacrifices, and endless praying for me.

Jinho Park

Washington University in St. Louis
August 2011

Contents

List of Tables

List of Figures

Chapter 1

Rapid Synthesis of Nanostructured Cu-TiO$_2$-SiO$_2$ Composites for CO$_2$ Photoreduction by Evaporation Driven Self-assembly[†]

1.1   Introduction

There are mounting concerns over the emission of greenhouse gases (GHG), in particular carbon dioxide (CO$_2$), which is one of the major contributors to global climate change.[1] A great deal of effort has been expended to reduce CO$_2$ emissions. For instance, the development of technologies to generate renewable energies is the most desirable way with regard to the long-term view.[2] However, in their current state, these technologies cannot fully replace the existing fossil fuel-based power generation. Thus, power generation via fossil fuel combustion with effective CO$_2$ capture, appears to become a key contributor to energy supply in the foreseeable future, which can be realized by pre-, post-, or oxy-fuel combustion processes.[3] The carbon dioxide capture and sequestration (CCS) processes, however, are energy-intensive and high-cost.[2]

Recent innovations have made photocatalysis technology a potentially promising alternative.[2, 4-6] The process can be applied for converting CO$_2$ to carbon-contained energy bearing compounds, such as carbon monoxide (CO), formic acid (HCOOH), methane (CH$_4$), methanol (CH$_3$OH), and ethanol (CH$_3$CH$_2$OH).

Another potential feature of the photocatalysis technology is that it can consume less energy in comparison to conventional methods by harnessing solar energy, which is abundant, cheap, and ecologically clean and safe.[2] In addition, a variety of inexpensive metal oxides, such as titanium oxide (TiO_2), are readily available as catalysts.

In spite of its economic and environmental benefits, the photocatalytic pathway suffers from low efficiency. A typical semiconductor-based photocatalyst needs to absorb light energy, generate electron-hole pairs, spatially separate them, transfer them to redox active species across the interface and minimize electron-hole recombination.[6] The decrease of the electron-hole recombination rate is a key factor in terms of enhancement of the photocatalytic activity. For this purpose, several methods have been proposed, including synthesis of catalysts with porous structures.[7-11] It is believed that the porous structure can effectively distribute the electron transfer, slow down the recombination rate, and hence enhance the photocatalytic performance. The other method is doping metals, such as copper (Cu) and iron (Fe) on the photocatalyst surface.[12, 13] The doping metal can absorb excited electrons, and thus separate electron-hole pairs to decrease the recombination rate.

The current photocatalysts, in particular, TiO_2-based inorganic catalysts with porous structures are intensively investigated, due to their unique morphology, high thermal stability, and improved photocatalytic efficiency. They are typically prepared by batch processes, such as hydrothermal, sol-gel, precipitation, impregnation or ion exchange methods.[7, 8, 10, 12, 14-18] The current photocatalysts for CO_2 reduction, however, do not perform as effectively as current solar hydrogen generation catalysts. The maximum CO_2 conversion rate was reported to be 25 μmol/g-TiO_2/hr.[6] Our recent results showed that the photoreduction efficiency could be improved by distributing Cu-TiO_2 nanocrystals inside a mesoporous silica (SiO_2) matrix prepared by a sol-gel method.[19] The catalysts prepared by these liquid methods, however, typically have an inhomogeneous phase distribution due to macroscopic reactions, leading to non-optimal performance. Further, these liquid methods generally need a very long time for both reaction and post treatments, such as surfactant/solvent removal and calcinations.

2

Thus they are difficult to apply to commercial scale production because of their high energy consumption and significant batch-to-batch variation. Therefore, it is essential to develop a process for the rapid preparation of Ti-based CO_2 photoreduction catalysts.

In this work, a rapid and direct synthesis of nanostructured copper-doped titania-silica (Cu-TiO_2-SiO_2) composite particles for CO_2 photoreduction using a furnace aerosol reactor (FuAR) method[20, 21] is demonstrated for the first time. The FuAR method is simple yet effective, with an extremely short processing time of several seconds.[22, 23] Catalyst particles are produced from micrometer-sized droplets, in which homogeneous phase distribution can be ensured by microscopic reactions inside the droplets. In addition, the FuAR method is applied in a continuous manner, avoiding batch-to-batch variations. The photocatalyst particles were prepared from aqueous suspensions of nanosized TiO_2 and SiO_2 colloids and copper nitrate solution, which are cheap and safe, and are readily available for mass production. The particle size, composition, structure, and hence the catalytic performance were tailored by manipulating precursor properties as well as process parameters. TiO_2 nanocrystals as the effective photocatalysts were efficiently utilized by selectively distributing them on the surface of silica mesoporous matrix by evaporation driven self-assembly[24-26] of these nanocolloids inside the micrometer-sized droplets, resulting in high CO_2 reduction efficiency.

1.2 Experimental Section

1.2.1 Catalyst Synthesis

The nanostructured Cu-TiO_2-SiO_2 composite particles were synthesized by the FuAR method, which is schematically shown in Fig. 1.1. The FuAR consisted of a 6-jet Collison nebulizer (BGI Instruments, Waltham, MA) as the atomizer, an electric furnace, a tubular alumina reactor, a microfiber filter, an air pump, and cooling and gas feeding systems. The schematic diagram of Cu-TiO_2-SiO_2 composite particle formation inside

the FuAR is shown in Fig. 1.2a. Aqueous suspensions of colloidal silica (Snowtex® OL, Nissan Chemical Industries, Ltd., Chiba, Japan) and titania (AERODISP® W740X, Evonik Degussa Corporation, Parsippany, NJ), and copper nitrate trihydrate ($Cu(NO_3)_2 \cdot 3H_2O$, 99.5% purity, Strem Chemicals, Newburyport, MA) aqueous solution were used as precursors. The precursors were atomized into micrometer-sized droplets by means of the atomizer, and the mist was delivered by air into the tubular alumina reactor (1 m in length and 25 mm in inner diameter) maintained at predetermined temperatures (from 400 to 1000 °C), followed by heating for several seconds. During the process, the micrometer-sized droplets underwent solvent evaporation, evaporation driven self-assembly of TiO_2 and SiO_2 nanocolloids, and further drying and pyrolysis of $Cu(NO_3)_2$ to form the final composite particles. These composite particles were collected downstream of the reactor using the glass microfiber filter (EPM 2000, Whatman Inc., Florham Park, NJ) for particle characterization and CO_2 photocatalytic reduction analysis.

The TiO_2 and SiO_2 nanocolloids were characterized by transmission electron microscopy (TEM) to determine size and morphology. From Fig. 1.2b, the TiO_2 nanocrystals, having an average diameter of 20 nm with an irregular shape, were clearly indentified in anatase phase (see inset in Fig. 1.2b); while the SiO_2 nanoparticles have an average diameter of 45 nm, which are amorphous with spherical morphology (Fig. 1.2c). The molar percentages of TiO_2 and $Cu(NO_3)_2$ to the total components were controlled from 0 – 100% and 0 – 2%, respectively. The total precursor concentration was varied from 0.001 to 0.1 M. All chemicals were used as received without further purification. Air was used as the carrier gas with a flow rate of 8 l/min (liter per minute at STP = 1.33×10^{-4} m^3/s). The Reynolds number (Re)[27] at 800 °C and 8 l/min, as an example, was calculated to be 183, indicating that the flow pattern inside the reactor was laminar (Re < 2000), without any random eddies, vortices and other flow instabilities. The residence time (τ_r) in this process is generally very short, and was estimated from the following equation assuming that the temperature distribution inside the reactor is uniform:[28]

$$\tau_r = \frac{\pi d^2 L}{4Q}\left(\frac{T_0}{T}\right)\left(\frac{1-y_w}{1-y_w^0}\right)$$

(1.1)

where d and L are inner diameter (m) and length (m) of the tube reactor, respectively, and Q is the inlet carrier gas flow rate (m^3/s). T_0 and T are room and heating temperatures (K), respectively. The term $(1-y_w)/(1-y_w^0)$ can be neglected since y_w, the molar fraction of water vapor in air is much smaller than 1 in the current work. As an example, τ_r was calculated to be 1.02 s at 800 °C with an inlet gas flow rate of 8 l/min at STP.
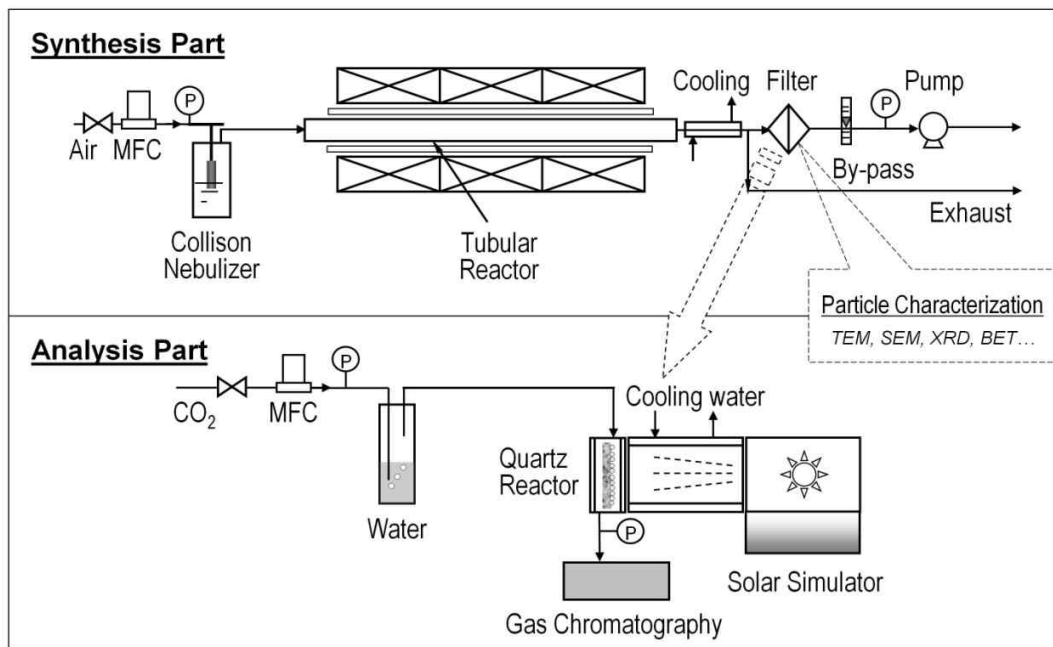
Figure 1.1.   **Schematic diagram of experimental setup for catalyst synthesis and analysis.**
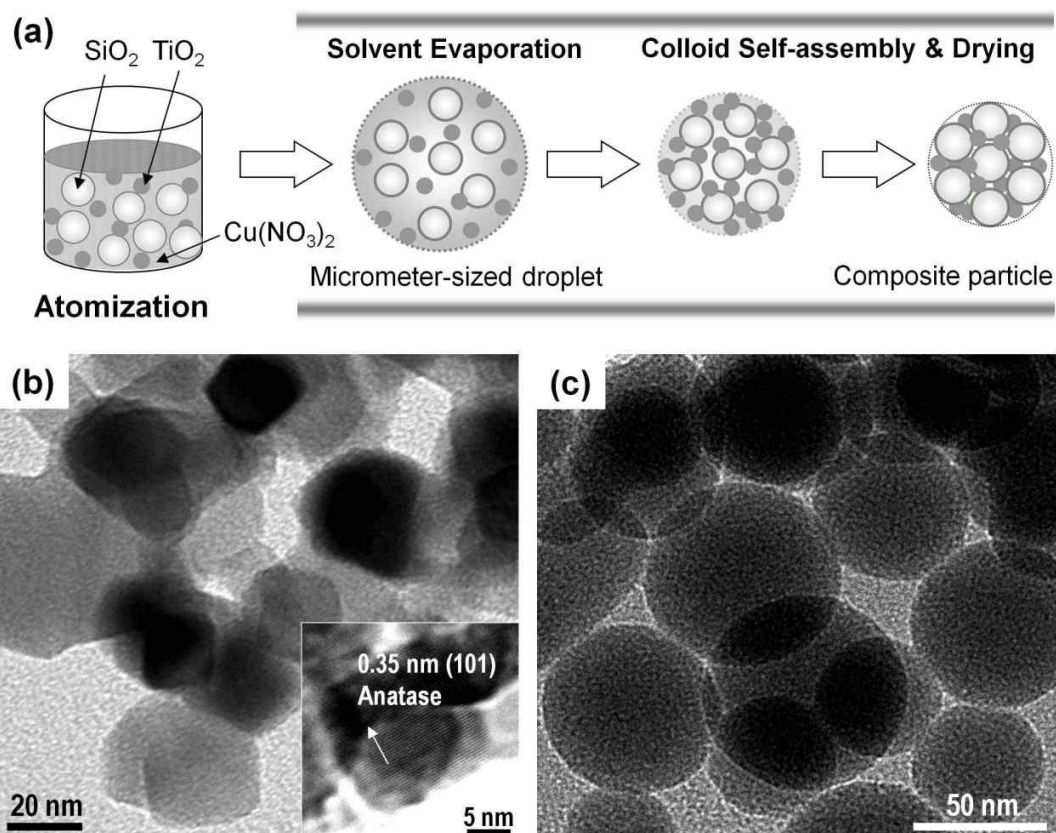
Figure 1.2. Cu-TiO₂-SiO₂ composite particle formation. (a) possible formation mechanism, and TEM images of (b) TiO₂ and (c) SiO₂ nanocolloids.

1.2.2 Composite Particle Characterization

The morphology and size of the composite particles were examined using field emission scanning electron microscopy (FESEM) (JSM-7001FLV, JEOL, Tokyo, Japan). The average diameters were determined by randomly sampling more than 300 particles from FESEM images. The inner structure was analyzed by TEM (JEM-2100F, JEOL, Tokyo, Japan). Before TEM analysis, the as-prepared particles were dried in a vacuum oven for 24 hours to eliminate any organic residues inside the mesoporous structure, which were then suspended in ethanol and followed by sonication for 30 min prior to being

dropped onto a TEM grid with a lacey support film. The crystal phase was determined by X-ray diffraction (XRD) (Geigerflex D-MAX/A, Rigaku Denki, Tokyo, Japan) using CuKa radiation (λ = 1.548 Å) at 30 kV and 30 mA, with a scan step of 0.02° in 2θ and a scan speed of 4°/min. The surface area and pore size distribution were analyzed using nitrogen physisorption method (Autosorb-1, Quantachrome Instruments, Boynton Beach, FL). In total, 79 adsorption and desorption points were analyzed. The surface area was calculated using Brunauer-Emmett-Teller (BET) method and the pore size distribution was obtained from the desorption isotherm, which is more appropriate than the adsorption isotherm for evaluating the pore size distribution of an adsorbent because for the same volume of gas, the desorption isotherm exhibits a lower relative pressure, resulting in a lower free energy state, i.e., closer to true thermodynamic stability.[29] The ultraviolet-visible (UV-VIS) spectra analysis was also performed (Cary 100, Varian, Inc., Palo Alto, CA), to check catalyst particles with different copper doping concentrations.

1.2.3 CO$_2$ Photoreduction Analysis

The photoreduction analysis system is shown in Fig. 1.1, which includes a home-made continuous flow reactor, a Xe arc lamp (Oriel 66021, Newport Co., Irvine CA), and a gas chromatography (GC) (6895N, Agilent Technologies, Inc., Santa Clara, CA). Compressed CO$_2$ (Instrument Gr. 4, Airgas, Inc., St. Louis, MO) was used as the source gas and the flow rate was controlled by a mass flow controller (MKS Instruments, Wilmington, MA). It passed through a water bubbler to generate a mixture of CO$_2$ and water vapor. The mixture was then introduced into the reactor, which was cylindrically built with a stainless steel wall and a quartz window vertically facing the solar lighter. The inner cavity was 60 mm in diameter and 25 mm in depth. Glass wool was placed in the reactor as the support for the glass fiber filter loaded with the catalyst particles. The glass wool supporter was moisturized with 3.0 g deionized water to maintain saturated water vapor in the reactor. The catalyst particles were illuminated by the Xe arc lamp which has an average light intensity of 2.4 mW/cm^2 for 250 nm < λ < 400 nm

measured by a spectroradiometer (ILT-900R, Polytec GmbH, Waldbronn, Germany). The concentrations of effluent gases (e.g. CO and CO_2) from the reactor were continuously measured by the GC through an automated gas valve, using helium (He) as the carrier gas. The GC was equipped with a 30 m × 0.32 mm PLOT capillary column (Supelco Carboxen-1010) and a thermal conductivity detector (TCD). Before each test, the reactor loaded with catalysts was first purged with CO_2 and water vapor at 100 ml/min for 1 hour and then the flow rate was reduced and maintained at 3.0 ml/min during the whole analysis process. After 30 minutes when the flow was stabilized, the Xe lamp was turned on and the concentrations of effluent gases as a function of irradiation time were recorded. The maximum concentration of CO gas was used as the CO yield.

1.3   Results and Discussion

The effect of synthesis temperature, an important parameter in the FuAR process determining the particle formation,[23] was first investigated. The composite particles were synthesized at various temperatures, i.e. from 400 to 1000 °C, by using the same precursor, that is, nanocolloidal TiO_2 and SiO_2 aqueous suspensions, with a TiO_2 molar percentage of 10% and a total precursor concentration of 0.05 M. As shown in the FESEM images in Fig. 1.3, the catalyst particles obtained at all temperatures had a spherical morphology, which was originated from the droplets whose spherical shape was maintained because of very low Bond number (much smaller than 1). [30]
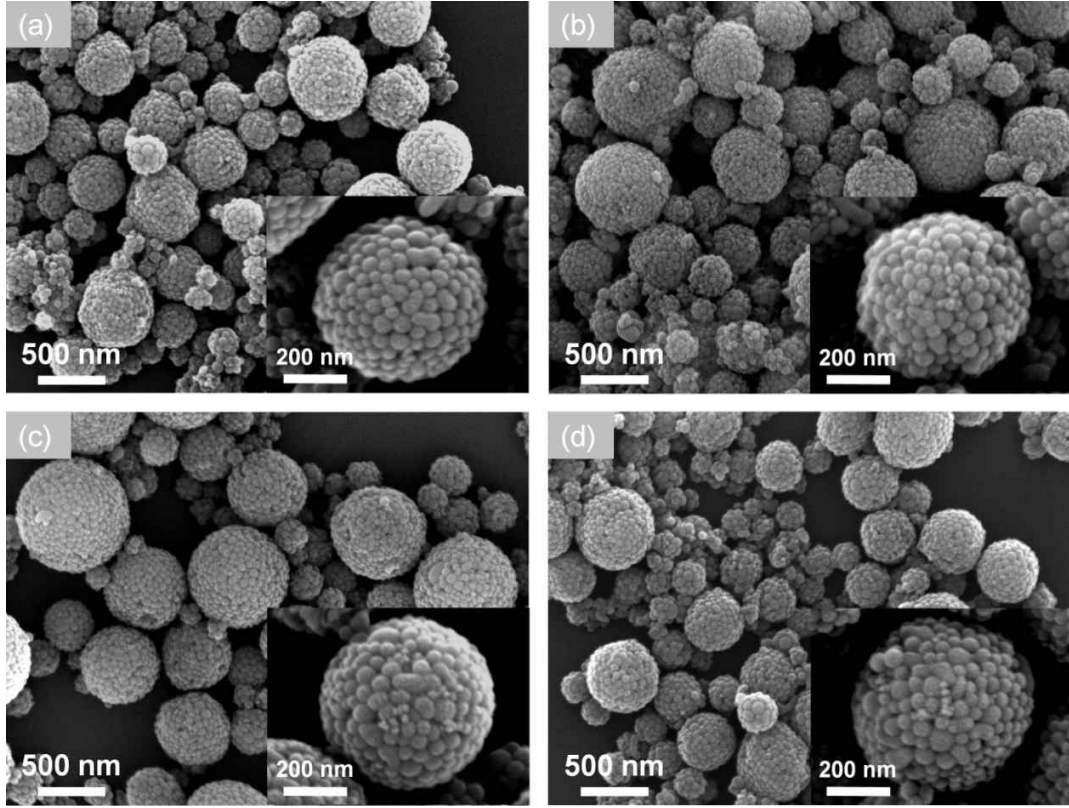
Figure 1.3. **FESEM images of TiO$_2$-SiO$_2$ composite particles prepared at different temperatures (a) 400, (b) 600, (c) 800, and (d) 1000 °C, with a fixed TiO$_2$ molar percentage of 10% and air flow rate of 8 l/min.**

The average diameters of the particles at each condition are almost similar, about 450 nm, since they were formed from the precursor with the same concentration. According to the typical one droplet to one particle (ODOP) principle, the estimated droplet size was calculated to be around 4 μm using the following equation: [31]

$$d_{\mathrm{p}} = d_{\mathrm{d}} \left(\frac{M_{SiO_2} C_{SiO_2}}{\rho_{SiO_2}} + \frac{M_{TiO_2} C_{TiO_2}}{\rho_{TiO_2}} \right)^{1/3}$$

(1.2)

where d_p and d_d are diameters (m) of product particles and droplets, respectively. M_{SiO_2}/M_{TiO_2}, C_{SiO_2}/C_{TiO_2}, and $\rho_{SiO_2}/\rho_{TiO_2}$ are molecular weights (kg/mol), molar concentrations (mol/m³), and densities (kg/m³) of SiO_2 and TiO_2, respectively. The composite particles shrank slightly at 1000 °C.[21, 22] But no significant sintering phenomenon of the nano-sized colloids was observed because the characteristic sintering or fusion time (τ_f) of these nanoparticles was estimated, for instance, around 2.86×10^2 s at 800 °C based on the following equation,[32] which is much longer than the corresponding residence time ($\tau_r = 1.02$ s) calculated using Eq. 1.1:

$$\tau_f = 5.98 \times 10^{13} d_p^3 T \exp\left(\frac{1.90 \times 10^4}{T}\right)$$

(1.3)

where d_p is the primary particle diameter of SiO_2 (m), and T is the synthesis temperature in Kelvin. This was also confirmed by the rough surface of the composite particles as shown in the above FESEM images as well as the detailed TEM analysis below, indicating that there is a possibility of porous structure formation in a laminar aerosol reactor in high temperature environment. TiO_2 nanocrystals were not included for the above estimation due to their extremely low molar percentages. Detailed information on sintering and residence times at various synthesis temperatures can be found in Table 1.1.

Figure 1.4 shows the representative TEM images of the particles obtained at 400 °C (Fig. 1.4a) and 800 °C (Fig. 1.4b). In Fig. 1.4a, one can find that the TiO_2 nanocrystals were evenly distributed inside the composite particle. Taking a close inspection on the particle surface, for example, in the spots of a_1 and a_2, most particles are spherical SiO_2 nanoparticles. Some TiO_2 nanocrystals were observed but not in large amounts. The composite is shown as the inset in the right corner of Fig. 1.4a. However, it is not the case for the particles obtained at 800 °C. In this case, more TiO_2 nanocrystals moved to the surface of the composite particle, which were clearly indicated by the magnified TEM images of b_1 and b_2 spots in Fig. 1.4b.

Table 1.1. **Effect of synthesis temperature on residence time, sintering time, specific surface area, pore diameter, evaporation rate, and CO yield**

Synthesis temperature (°C)	Residence time (s)	Sintering time (s)	Specific surface area (m^2/g)	Pore diameter (nm)	Evaporation rate (g/s)	CO yield (mol/g-TiO_2/hr)
400	1.63	6.65×10^6	87.03	33.7	6.79×10^{-8}	3.66
600	1.26	1.34×10^4	82.31	32.2	1.04×10^{-7}	4.89
800	1.02	2.86×10^2	72.38	28.3	1.50×10^{-7}	8.24
1000	0.86	2.10×10^1	70.35	23.8	1.77×10^{-7}	6.82

(a)

100 nm

(a₁)

TiO₂

50 nm

(a₂)

SiO₂   TiO₂

10 nm

12
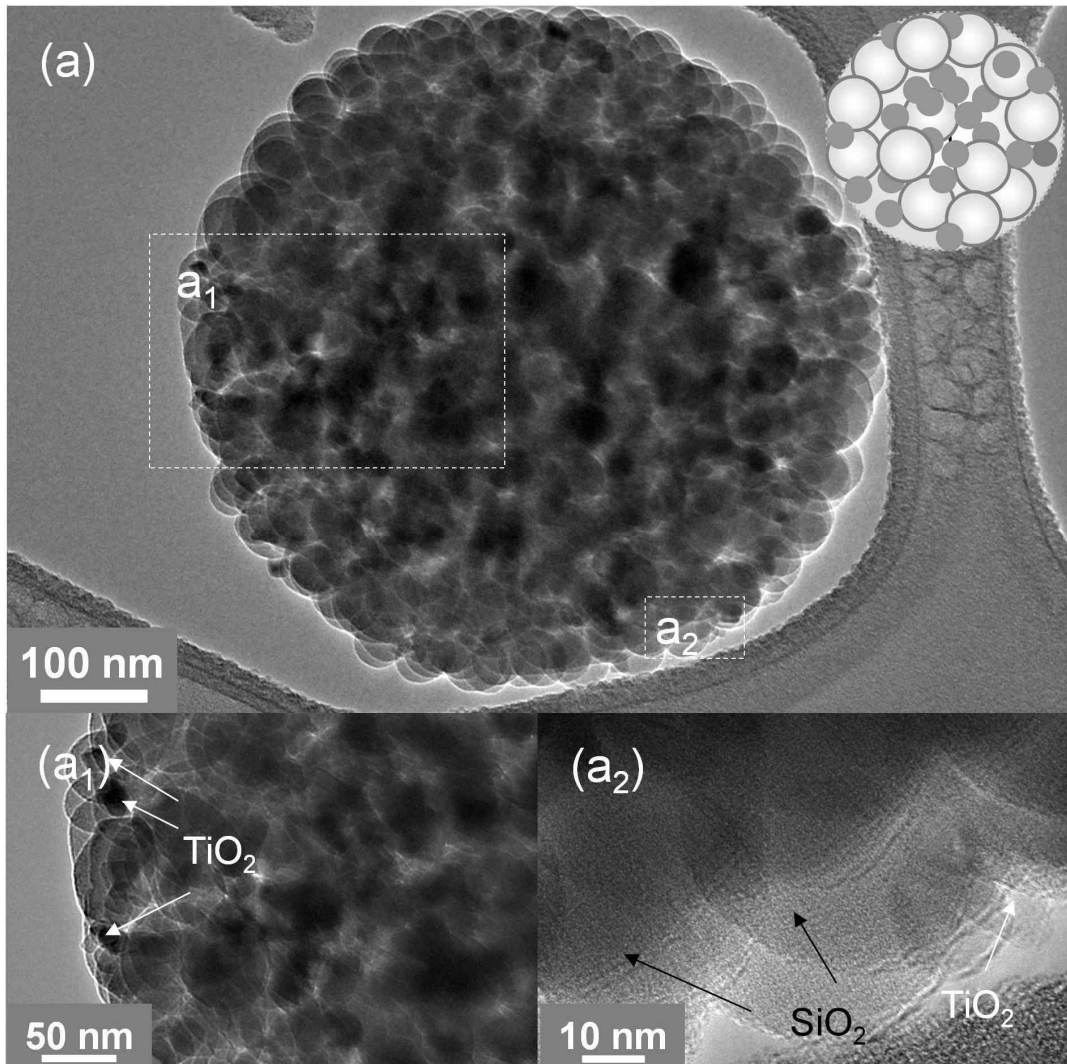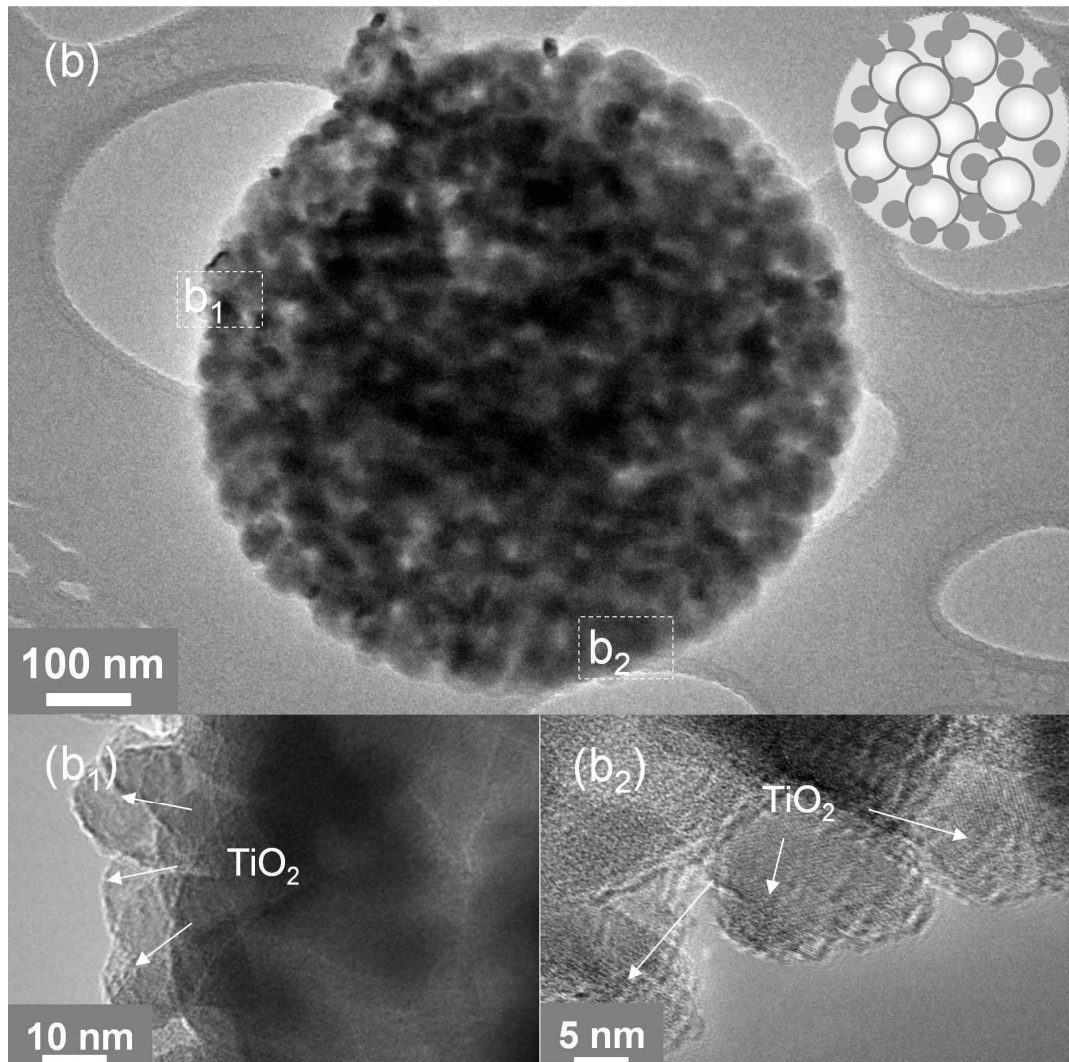
Figure 1.4. TEM and HR-TEM images of TiO$_2$-SiO$_2$ composite particles prepared at 400 and 800 °C shown in Fig. 1.3. The insets are schematic diagrams of the composites, in which the white ball represents SiO$_2$ and the black spot indicates TiO$_2$.

The phenomenon was attributed to the droplet evaporation at high temperatures.[24, 33] In a FuAR route, it has been demonstrated that for a droplet containing colloids with different sizes, colloids with smaller size can move towards the surface of the droplet faster than the larger ones, since smaller particles have higher mobility.[33] For example,

the TiO_2 nanocrystals in this work have a smaller size than that of the SiO_2 nanocolloids, which can be expected to move faster than the SiO_2 colloids to the droplet surface. The driving force of the movement is the local temperature gradient at the surface of the micrometer-sized droplet created by the solvent evaporation due to the high temperature heating. In general, as a droplet evaporates, a non-uniform temperature distribution, i.e. a temperature drop is established by heat loss due to the phase change from liquid to vapor at the evaporating surface.[26, 34] For common fluids, such as water, the surface tension increases with a decreasing temperature. As a result of the surface tension gradient as well as the thermophoretic force, the liquid interface is "pulled" toward the colder regions, i.e. the droplet surface. Viscous drag moves the fluid adjacent to the surface, and consequently, surface-tension-driven Marangoni flow is initiated.[35] The solvent evaporation rate can be enhanced at a higher temperature for droplets evaporated at different temperatures, creating a stronger evaporating cooling effect,[34] moving more TiO_2 nanocrystals to the composite particle surface. Evaporation rates under different synthesis temperatures are shown in Table 1.1.

The above composite particles were also subjected to physisorption measurement to determine the surface area, pore size, and its distribution. Figure 1.5 shows the adsorption and desorption isotherms of the composite particles prepared at 800 °C and 8 l/min, which can be assigned to be Type V, a typical type for mesoporous structure. The isotherms also show A type hysteresis, indicating their cylindrical pore structure.[29] The corresponding pore size distribution is shown as the inset, which reveals that the average pore size of the composite particles is approximately 28 nm. It should be noted that the mesoporous structure was directly formed in the FuAR process without using any templates avoiding contamination and reducing costs. The surface area and average pore size as a function of synthesis temperature were summarized in Table 1.1. It is apparent that both surface area and average pore size decrease with increasing synthesis temperature. For example, the surface area and average pore size at 400 °C were 87.03 m^2/g and 33.7 nm, respectively; while the corresponding data for 1000 °C were decreased to 70.35 m^2/g and 23.8 nm, respectively. The phenomenon was attributed to the shrinkage at high temperatures as explained before.
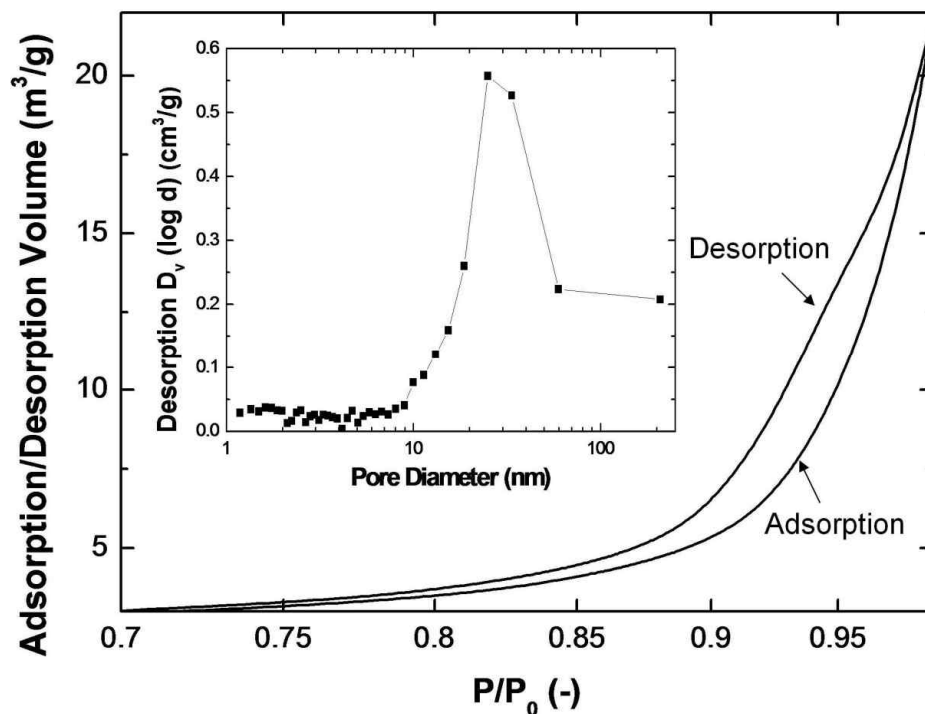
Figure 1.5. Representative nitrogen adsorption/desorption isotherm of TiO_2-SiO_2 particles synthesized at 800 °C with a fixed TiO_2 molar percentage of 2%. The inset is the pore size distribution calculated from the desorption isotherm.
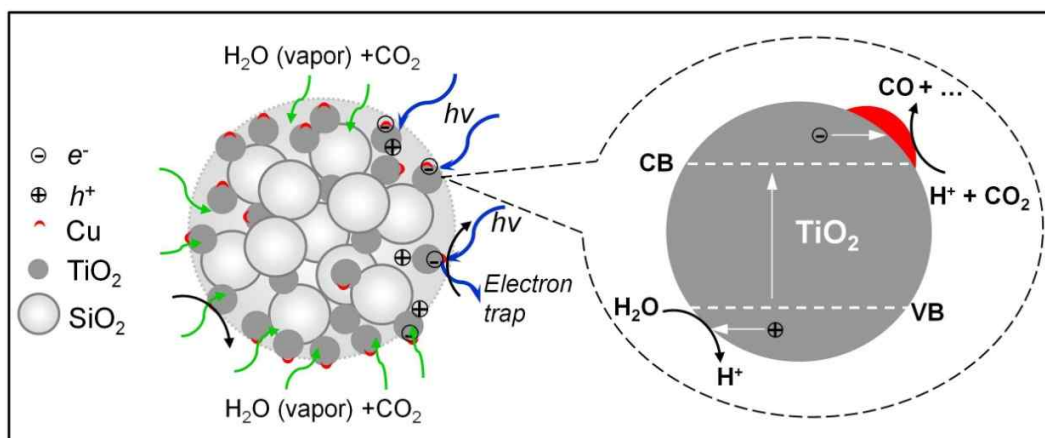
Figure 1.6. Proposed photoreduction pathways of mesoporous Cu-TiO_2-SiO_2 composite particles.

The photoreduction analysis was then carried out for these composite particles. The possible pathways for the photoreduction of CO_2 by the mesoporous Cu-TiO_2-SiO_2 particles are schematically shown in Fig. 1.6. As explained in the experimental section, the photoreduction of CO_2 was conducted in a reactor where a mixture of CO_2 and water vapor was presented. The mixture first diffused into the porous structure of the composite particle and then adsorbed on the TiO_2 nanocrystal surface. Upon illumination by the UV light, the TiO_2 got activated to generate electron-hole pairs for the reaction. The electron-hole pairs were then spatially separated and distributed inside the porous structure to slow down the electron-hole recombination. In addition, Cu doped on the TiO_2 surface can trap electrons to separate the pairs and hence enhance the photoreduction efficiency. The photoreduction of CO_2 happened in the third step, in which the electrons were transferred to the TiO_2 nanocrystal surface to react with CO_2 and water vapor to form various products, such as CO, CH_4, $HCOOH$, CH_3OH, and even CH_3CH_2OH. The mechanism of photoreduction of CO_2 is quite complex.

The reduction of CO_2 by one electron to form $\cdot CO_2^-$ is highly unfavorable, having a reduction potential of -2.14 V vs SCE.[36] Most of the researchers now agree that this process is based on proton-assisted multi-electron transfer (MET) mechanism (see Appendix A for details).[36, 37] Based on the MET mechanism, although the formation of methane, methanol, and ethanol is thermodynamically favorable, it requires more electrons and protons. These products are more likely produced in CO_2 photoreduction in aqueous solutions, since more protons can be supplied by water.[12, 18] Since this study focused on CO_2 reduction on a gas-solid interface, CO was found as the main product in our flow reactor system as it needs minimum number of electrons and protons. CO also has significant fuel value ($\Delta_c H° = $ -283.0 kJ mol^{-1}) and can be readily converted into methanol for use as a liquid fuel.[38] CO yield was investigated systematically as functions of synthesis temperature, TiO_2 molar percentage, Cu molar percentage, as well as precursor concentration.

Table 1.1 shows the synthesis temperature effect on the CO yield of TiO_2-SiO_2 particles with a TiO_2 molar percentage of 2%. From the table, the CO yield first increased from 3.66 μmol/g-TiO_2/hr at 400 °C to 4.89 μmol/g-TiO_2/hr at 600 °C. After reaching the maximum, i.e. 8.24 μmol/g-TiO_2/hr at 800 °C, it slightly decreased to 6.82 μmol/g-TiO_2/hr at 1000 °C. The increase of CO yield from 400 to 800 °C was due to the increased quantity of TiO_2 nanocrystals on the mesoporous SiO_2 matrix surface, which was clearly evidenced by the TEM images and explained as shown before. The slightly decreased CO yield at 1000 °C was due to the decrease in surface area and pore size, as indicated in Table 1. It is believed that the decreased surface area and pore size of the composite catalyst particles would limit the adsorption of the CO_2 and water vapor mixture on the catalyst particle surface and hence resulted in a relatively low CO yield.

The effect of TiO_2 molar percentage was investigated as well. Figure 1.7a indicates that the CO yield first increased with increasing TiO_2 molar percentage. After it reached the maximum value of 8.24 μmol/g-TiO_2/hr at 2%, it decreased significantly. Only 1.51 μmol/g-TiO_2/hr could be achieved at the TiO_2 molar percentage of 10%, and an even lower value of 0.1 μmol/g-TiO_2/hr was obtained when using pure TiO_2. The reason was caused by agglomeration of the primary TiO_2 nanocrystals during the synthesis. In general, the agglomeration rate increases with increasing particle number concentration.[39] For instance, in the case of using 100% TiO_2 nanocrystals, the final composite particles are actually agglomerate spheres of individual TiO_2 nanocrystals with the average diameter of several hundred nanometers. In the agglomerates, the probability of electron-hole recombination would increase on the interfaces of individual TiO_2 nanocrystals. However, in the case of low TiO_2 molar percentages, less agglomeration would happen and isolated individual TiO_2 nanocrystals would be mainly distributed on the surface of the porous SiO_2 matrix, eliminating the surface and volume electron-hole recombination,[2] thus enhancing the photoreduction efficiency.
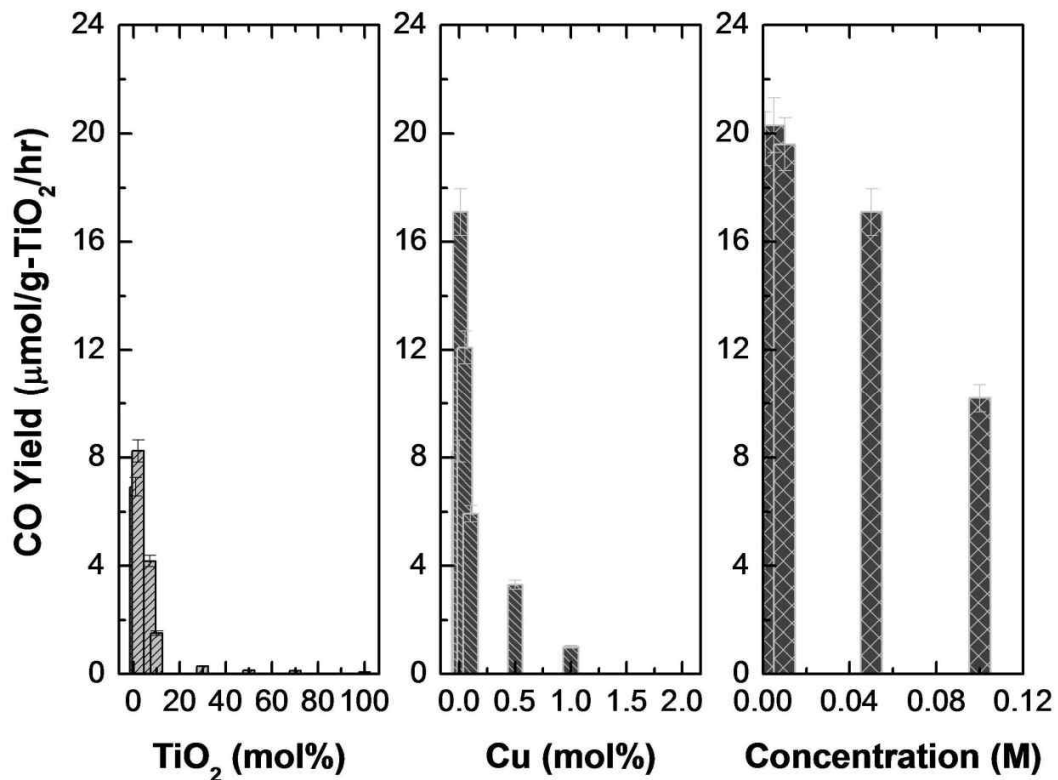
Figure 1.7. CO yield as functions of various parameters. (a) TiO₂ molar percentage, (b) Cu molar percentage, and (c) total precursor concentration. The synthesis temperature and air flow rate were fixed at 800 °C and 8 l/min.

As demonstrated above, a maximum CO yield, i.e. 8.24 μmol/g-TiO$_2$/hr was obtained by using an optimal TiO$_2$ molar percentage of 2%. The value, however, is still very low in comparison to the previous research. In order to improve the reduction efficiency, copper doping was carried out to further decrease the electron-hole recombination rate. To check the doping effect, the TiO$_2$ molar percentage and temperature were fixed at 2% and 800 °C. Figure 1.7b shows that similar to that of TiO$_2$ molar percentage effect, there is an optimal Cu molar percentage at 0.01%, in which a high CO yield of 17.1 μmol/g-TiO$_2$/hr was achieved. After that, the CO yield, however, decreased with increasing Cu molar percentage. It was probably due to the formation of CuO which

covered the porous silica surface as well as TiO_2, preventing the direct contact of CO_2 and TiO_2.

To further explore the reduction efficiency, the effect of total precursor concentration was also investigated as shown in Fig. 1.7c. Based on Eq. 1.3, one can easily know that the particle size increases with increasing precursor concentration, assuming that the droplet size is the same, which was proved by previous research.[40] The particle size as a function of total precursor concentration was presented in Table 1.2. It monotonically increased from 123 nm at 0.001 M to 571 nm at 0.10 M. It is also apparent from Table 1.2 that the number of individual TiO_2 nanocrystals per composite particle increased with increasing total precursor concentration, indicating the increased probability of agglomeration of these individual nanocrystals, which is considered as one of the reasons for deteriorated photoreduction efficiency. The highest CO yield achieved was as high as 20.3 μmol/g-TiO_2/hr at 0.05 M. Besides the agglomeration reason explained above, the specific surface area effect is also another major reason, since the specific surface area of the particles generally increases with decreasing particle size.

Table 1.2.   **Effect of concentration on particle size and CO yield**

Precursor concentration (M)	Particle diameter (nm)	N_{TiO2}* (#/particle)	Specific surface area (m^2/g)	CO yield (μmol/g-TiO_2/hr)
0.001	123	3	92.54	19.2
0.005	210	15	88.32	20.3
0.01	265	31	81.71	19.6
0.05	453	155	72.38	17.1
0.1	571	310	65.46	10.2
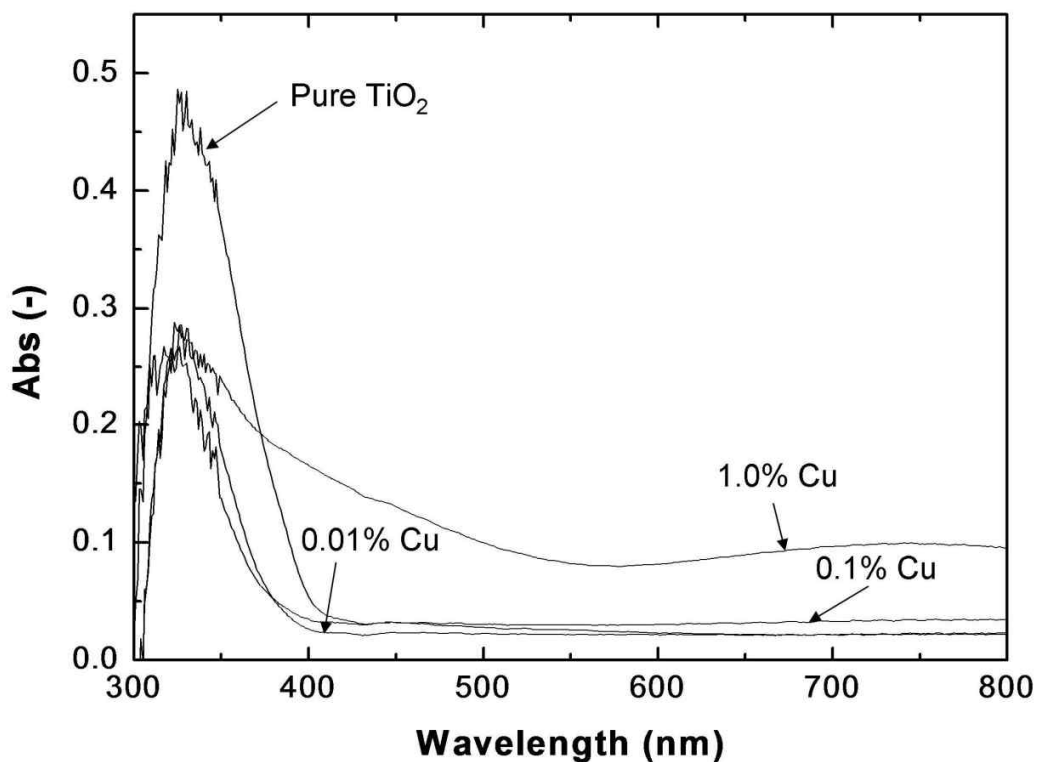
Figure 1.8. UV-VIS spectra of the as-prepared composite particles with different Cu molar percentages. The particles were obtained with TiO$_2$ molar percentage of 2% and an air flow rate of 8 l/min at 800 °C.

To explain the effect of copper doping effect, UV-VIS spectra was also analyzed for the catalyst particles with different copper doping concentrations (Fig. 1.8). The TiO$_2$ molar percentage was fixed at 2%, while the copper molar percentages were varied from 0 to 1%. For pure TiO$_2$-SiO$_2$, the absorption peak wavelength was located at around 367 nm, which is slightly shorter than the standard absorption wavelength of bulk anatase, i.e. 387 nm, due to the quantum size confinement (blue shift) of nanosized TiO$_2$. With Cu doping up to 0.1%, there is no significant bandgap shift due to the very low doping concentration. In addition, no absorption peaks in the visible range could be observed for all of the above three cases. However, the absorption in the visible range was observed when increasing Cu molar percentages from 0.1 to 1%. This was due to the

formation of CuO (E_b = 1.2 eV) inside the particles, which was the reason for the decreased photoreduction efficiency as explained before.

1.4   Conclusions

Cu-TiO$_2$-SiO$_2$ mesoporous composite particles were successfully synthesized by the FuAR method in a rapid manner. The size, composition, and porosity of the composite particles were tailored by manipulating the precursor concentration, stoichiometric ratio, and temperature profile, respectively. The results revealed that the as-prepared particles were submicrometer-sized mesoporous spheres having optimal molar percentages of TiO$_2$ and Cu to the whole particle of 2% and 0.01%, respectively. The TiO$_2$ nanocrystals were efficiently utilized by selectively distributing them on the SiO$_2$ mesoporous matrix surface by evaporation driven self-assembly, resulting in a relatively high CO$_2$ conversion efficiency with a maximal CO yield of approximately 20 μmol/g-TiO$_2$/hr. It should be noted that these catalyst particles were obtained within merely several seconds, much faster than those by time/energy consuming wet-chemical methods. The mesoporous structure was directly formed inside the FuAR process without any templates and post-treatment, thus avoiding contamination and reducing cost.

Chapter 2

Inactivation of *E. coli* in Water using Photocatalytic, Nanostructured Films Synthesized by Aerosol Routes[†]

1.1   Introduction

Currently, nearly 20% of the world's population lacks clean drinking water.[41,42] Couple this fact with a rapidly increasing world population, and the pressing need for clean water supplies becomes obvious. Many groundwater and surface water sources are too contaminated to drink directly thus necessitating safe and reliable disinfection techniques.[43] Conventionally, water has been disinfected by chlorination which uses free chlorine as a strong oxidant.[44] This biggest drawback to this method is the production of carcinogenic disinfection by-products (DBPs) such as trihalomethanes and haloacetic acids.[45] Ozone can also be used as a strong oxidant for disinfection of water. However, ozonation also has the potential to produce toxic DBPs during the disinfection process.[46] Therefore, safe and sustainable alternative water disinfection technology is strongly required.

Photocatalytic disinfection is considered a promising alternative due to several inherent advantages. First of all, photocatalytic disinfection does not produce any toxic carcinogenic DBPs. Photocatalytic materials used for disinfection can be recycled while the conventional methods consume chemical disinfectants. In addition, titanium dioxide (TiO_2), the typical photocatalytic material used, is non hazardous. Moreover, oxidants generated by photocatalytic materials are strong enough to inactivate pathogenic microorganisms in water.[47]

TiO_2 nanoparticles have been studied mainly as a photocatalytic material for inactivation of pathogenic microorganisms such as bacteria, viruses, algae and fungi because they have several useful qualities: large surface area, thermal and chemical stability, and are rather inexpensive materials.[48-52] In 1985, Matsunaga et al. have first studied photocatalytic inactivation. They inactivated *L. acidophilus*, *Sm. cerevisiae* and *E. coli* using TiO_2 particle suspension.[48] Wei et al. (1994) used P25 (TiO_2, Degussa) to inactivate *E. coli* in water. They reported effects of particle dosage, light intensity etc. on the inactivation rate.[49] Hu et al. (2006 and 2007) have synthesized Ag/TiO_2 and $Ag/AgBr/TiO_2$ composites to inactivate bacteria under irradiation of visible light.[50,51] However, TiO_2 nanoparticles must still overcome a number of challenges before replacing conventional water disinfection methods. First, TiO_2 nanoparticles must be removed from disinfected water post-treatment. Unfortunately removing nano-sized particles from liquid is very difficult and energy expensive. Secondly, particle suspensions in water can block light, an essential aspect for photoactivation. In addition, inactivation efficiency is still low because electron-hole (e-h) pairs generated by photoactivation recombine quickly.[47,53]

Thus, in order to overcome these problems, some research groups have studied inactivation of pathogenic microorganisms using immobilized TiO_2 films.[54-57] Photocatalytic inactivation using an immobilized TiO_2 film alleviates post-treatment removal of nanoparticles and does not cause light blockage. Kuhn et al. (2003) have reported inactivation of *E. coli*, *P. aeriginosa*, *S. aureus*, *E. faecium* and *C. albicans* using P25-coated glass under UV light.[55] They investigated susceptibility of the bacteria, which was

shown as follows: *E. coli* > *P. aeriginosa* > *S. aureus* > *E. faecium* > *C. albicans*.[55] Sunanda et al. also investigated inactivation of E. coli using a dip-coated TiO_2 film.[56] To enhance inactivation rate, Reddy el al. prepared TiO_2 coated on zeolite for use of inactivation of *E. coli*.[57]

Recently, a few research groups have studied the photoelectrochemical inactivation by applying electric potential on the TiO_2 film to separate well e-h pairs to reduce their recombination rate[58,59] Yu et al. prepared a Ti-based photocatalytic film by electrodeposition and investigated the photoelectrochemical inactivation of *E. coli* by applied voltage on the film.[58] Heyden el al. also studied both photochemical and photoelectrochemical inactivation of *E. coli* using a quantum dot-deposited TiO_2 nanotube film.[59]

In use of TiO_2 films for photochemical and photoelecrochemical reaction, the morphology of the TiO_2 film is known as one of the most important factors.[60] However, the effect of the morphology of the film on efficiency of photocatalytic inactivation of microorganism has not been dealt yet systemically. Therefore, in this study inactivation of the pathogenic microorganisms using TiO_2 films having different morphology is investigated. *Escherichia coli* (*E. coli*) was selected as pathogenic microorganisms in the study because it is one representative indicator of contamination of water.[53] Several morphological TiO_2 films were synthesized via aerosol chemical vapor deposition (ACVD) method. The ACVD has been reported as a single-step novel process to synthesize nanostructred metal oxide films with well controlled morphologies, which can be also easily scaled-up.[61,62] This study describes the effect of film morphology on the efficiency of inactivation of *E. coli* in water using different morphological TiO_2 films: columnar, granular and branched structures. In addition, the effect of applied voltage on the phototalytic inactivation is also investigated.

2.2 Experimental Section

2.2.1 Preparation and Characterization of TiO$_2$ Films by ACVD

TiO$_2$ films having different morphologies were prepared by ACVD method. Titanium tetraisopropoxide (TTIP, Sigma-Aldrich) was used as a precursor for synthesis of the films. Tin-doped indium oxide (ITO) coated aluminostilicate glass (Delta Technologies, Stillwater) was selected as a substrate for deposition of the TiO$_2$ films. Synthesis of TiO$_2$ films via the ACVD method has been described by An et al.[61,62] Process parameters for each morphology: columnar, granular and branched structure are summarized in Table 2.1.

Table 2.1. Summary of Experimental Parameters for Synthesis of TiO$_2$ Films via ACVD

Test	Morphology	Temperature of substrate [°C]	Precursor feed rate [μmol/min]	Particle ratio [%]	Residence time [ms]	Deposition time [min]
1	Columnar	500	1.53	13	20	50
2	Granular	450	4.34	30	53	70
3	Branched	450	4.34	18	30	23

A field emission scanning electron microscope (FESEM, Nova 2300, FEI) and a transmission electron microscope (TEM, Spirit Lab6, FEI) were used for morphology and thickness characterization of as-prepared films. Crystal structure of as-prepared TiO$_2$ films was characterized using an x-ray diffractomer (XRD, Geigerflex D-MAX-A, Rigaku) with Cu-Kα radiation at 35 kV and 35 mA. XRD patterns of columnar, granular and branched structured films were scanned from 20 to 60 ° of 2θ. A UV-Vis spectroscope (Cary 100, Varian) was used for absorption spectra of as-prepared films

across the ultraviolet and visible light spectrum. Bandgap energy of the films was obtained from their UV-Vis absorption spectra by plotting the correlation between photon energy (hν) and $(\alpha_{KM}h\nu)^{0.5}$. α_{KM} is the light absorption coefficient of the TiO_2 films calculated using the *Kubelka-Munk* formalism which is expressed as: [63]

$$\alpha_{KM} = \frac{(1-R_\infty)^2}{2R_\infty}$$

(2.1)

where R_∞ is reflectance of an infinitely thick sample. Since TiO_2 is an indirect semiconductor, bandgap energy can be obtained from the linear correlation between photon energy and square root of the absorption coefficient.[63]

2.2.2 Estimation of Surface Area of TiO_2 Films

Total surface area of each film type was estimated by mimetic methods. It was conducted to figure out surface area of the TiO_2 film of different morphologies and the effect of surface area on the inactivation rate. For the columnar film, a column was considered as a cone shape (Fig. 2.1(a)) and arrangement of columns on the film was assumed as the hexagonal packing of circles (Fig. 2.1(b)). The granular structure was mimicked with two cases: Granular film-1 and Granular film-2 (See Fig. 2.1(a)). Granular film-1 was considered the granular structure as deposition of a single layer of small primary particles on the column. Arrangement of a single layer of primary particles on the lateral surface of the column was also considered as the hexagonal packing. On the other hand the granular structure was assumed as bunch of primary particles in the boundary of the column in Granular film-2. Small primary particles in the column boundary were arranged as the hexagonal close packing of spheres (Fig. 2.1(c)). In case of the branched structure the film cone-shaped columns with also cone-shaped branches on their lateral surface as shown in Fig. 2.1(a). The cone-shaped branches on the lateral surface of the column were arranged as the hexagonal packing of circles (Fig. 2.1(b)).

27

(a) Columnar film   Granular film-1, 2   Branched film

(b) Hexagonal packing arrangement of circles
(Packing density = 0.9069)

Film

Columns on a film

Lateral surface of a column

Primary particles or Branches on a column

(c) Hexagonal close packing of spheres
(Packing density = 0.7405)

Primary particles in a column
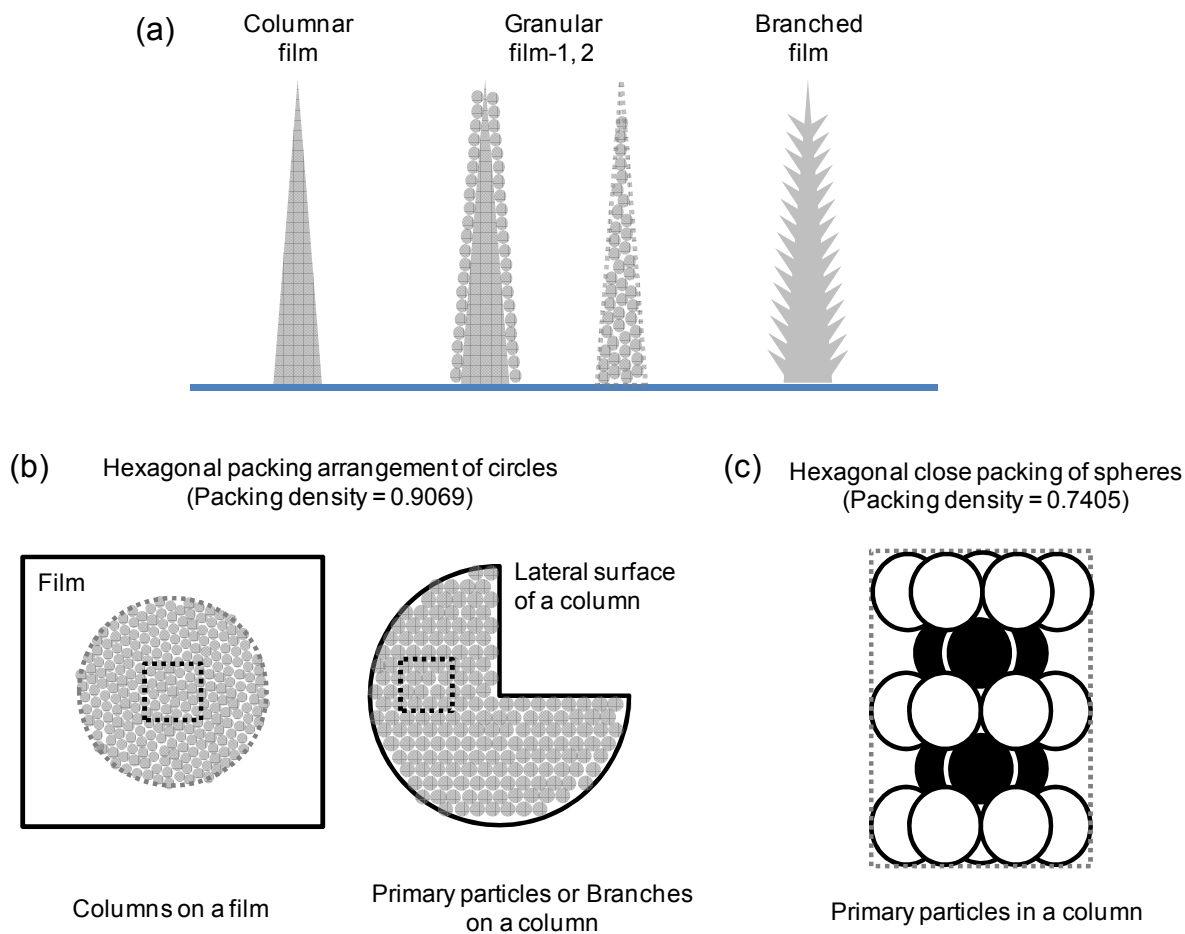
Figure 2.1. Estimation of surface area of a columnar, a granular, and a branched film. (a) Mimetic shapes of the columnar, granular and branched film. (b) Hexagonal packing arrangement of circles describing arrangement of plane bases of columns on the film and primary particles or plane bases of branches on the lateral surface of a column. (c) Hexagonal close packing of spheres for description of arrangement of primary particles in a column.

Table 2.2. Dimensions for Estimation of Surface Area of Films

Diameter of deposition area of a film	11 mm
Height of a column	20 μm
Diameter of base circle of a column	0.5 μm
Diameter of primary particles of the granular structure	15 nm
Height of a branch	125 nm
Diameter of base circle of a branch	25 nm
Hexagonal packing density of circles	0.9069
Hexagonal close packing density of spheres	0.7405

Dimensions for the deposited area of the film, the single column, the single primary particle and the single branch were determined from their photos and electron microscope images, which are described in Table 2.2.

2.2.3   Culture and Sampling Cells

E. coli, a Gram-negative was cultured for 18 h in growth medium at 37 °C. Growth medium was prepared by dissolving 25 g of Luria-Bertani broth powder (LB broth, Difco) in 1 L of deionized (DI) water and autoclaving for 50 min at 121 °C. During culturing *E. coli* optical density at 600 nm (OD_{600}) of culture solution was measured

every hour to establish the saturation point of *E. coli*. As shown in Fig. 2.2, *E. coli* cultures reached saturation after 18 hours at a concentration of 1.4×10^9 cells/mL.
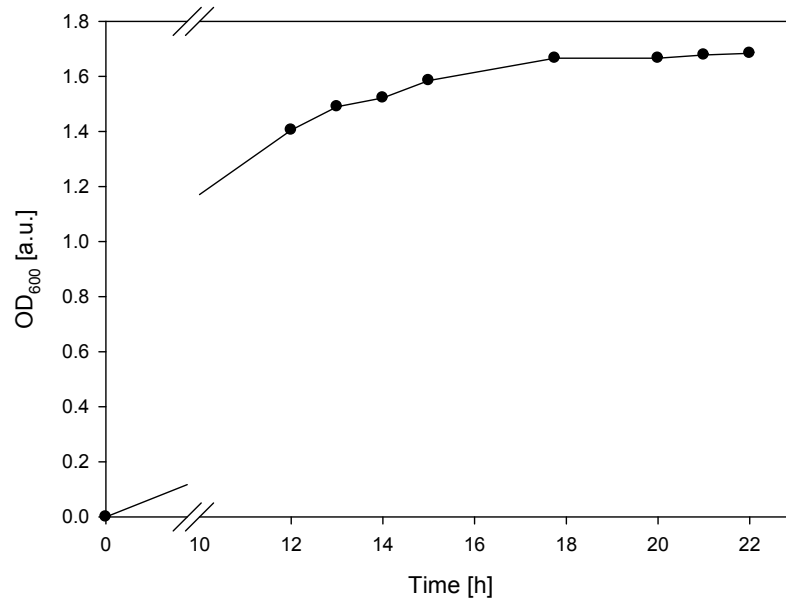
Figure 2.2. OD$_{600}$ of *E. coli* culture solution measured at different culture time.

Culture solution was sampled at saturation point (18 h) and cells were pelleted by centrifugation for 10 min at 3000 rpm. Pelleted cells were suspended in 50 mL of buffer solution (5.0 mM sodium sulfate) creating a working cell suspension with a concentration of approximately 10^8 cells/mL. Viable *E. coli* concentration was determined from heterotrophic plate counts as serial dilution of samples were plated on nutrient agar (LB agar, Difco) followed by incubation for 12 h at 37 °C. Each sample was plated in triplicate.

2.2.4   Light and Material Control

In order to determine the direct effect of light on *E. coli* viability, a light control was conducted. An arc Xe lamp (Oriel) was used as the light source and was operated by a 450 W power supply (E3630, Oriel). A water filter was attached to the lamp to remove

infrared light. *E. coli* solution was irradiated by arc Xe lamp and 100 μL solution was sampled at 0, 30, 60, 90 and 120 min. In order to cut off strong ultra violet (UV) light (UVB and UVC) a blue band pass filter was attached and effect of light on *E. coli* cells with and without the blue band pass filter was compared. In addition, light intensity of the lamp was measured using a spectroradiometer (RPS900, International Light) with and without the blue band pass filter to verify that it can effectively remove the strong UV wavelengths. UVB and UVC was reported as strong as they can inactivate some microorganisms by themselves.[64] Thus, in order to clearly investigate inactivation of *E. coli* by photochemical and photoelectrochemical reaction, effect of UV on the *E. coli* needs to be minimized.

The effect of non-irradiated nanostructured TiO_2 films on *E. coli* viability was also examined. As-prepared TiO_2 film soaked into the 50 mL of *E. coli* solution and samples taken at 0, 30, 60, 90 and 120 min. Especially, 0.8 V of external voltage was applied on TiO_2 film to determine the effect of TiO_2 film with electric bias. During the material control a reactor was covered with aluminum foil to block ambient light.

2.2.4   Photochemical and Photoelectrochemical Inacitvation of *E. coli*

Photochemical and photoelectrochemical inactivation of *E. coli* was conducted as shown in Fig. 2.3. For the photochemical inactivation, only the TiO_2 film soaked in the *E. coli* solution (no platinum wire was used). For photoelectrochemical inactivation, both TiO_2 film and platinum (Pt) wire soaked in solution while 0.8 V electric potential was applied between the two electrodes using a sourcemeter (SourceMeter 2400, Keithley) for photoelectrochemical inactivation. The arc Xe lamp was used as light source at 450 W with the water and the blue band pass filters in place. *E. coli* solution in the inactivation reactor was sampled at 0, 5, 10, 15, 20, 30, 60 and 120 min.
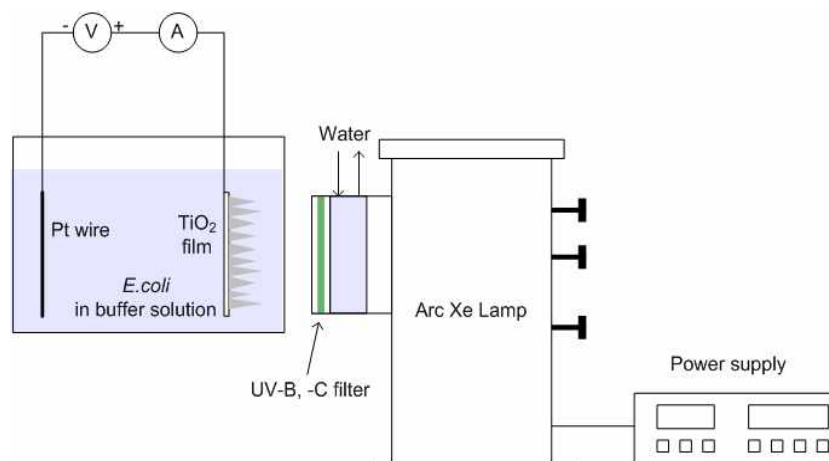
Figure 2.3. A schematic diagram of the experimental setup used for photochemical and photoelectrochemical inactivation of *E. coli*.

2.3   Results and Discussion

Figure 2.4 shows SEM and TEM images of as-prepared columnar, granular and branched TiO_2 films. In all cases, thickness of films was well controlled around 2 μm. In Figs. 2.4 (a), (b) and (c), it is shown that TiO_2 was well developed in one direction without any grains or branches. In addition, the tip of the single column is very sharp meaning that TiO_2 monomers or small primary particles deposited on the film were completely sintered, thereby forming a single column. Granular structure was composed of bunch of small grains while branched structure has some sharp branches on its surface which were composed of well sintered grains. Moreover TEM images of both structures make it more clearly (Figs. 2.4(f) and (i)). In case of granular TiO_2, small grains are well observed whereas 1-D branches are shown in branched TiO_2.
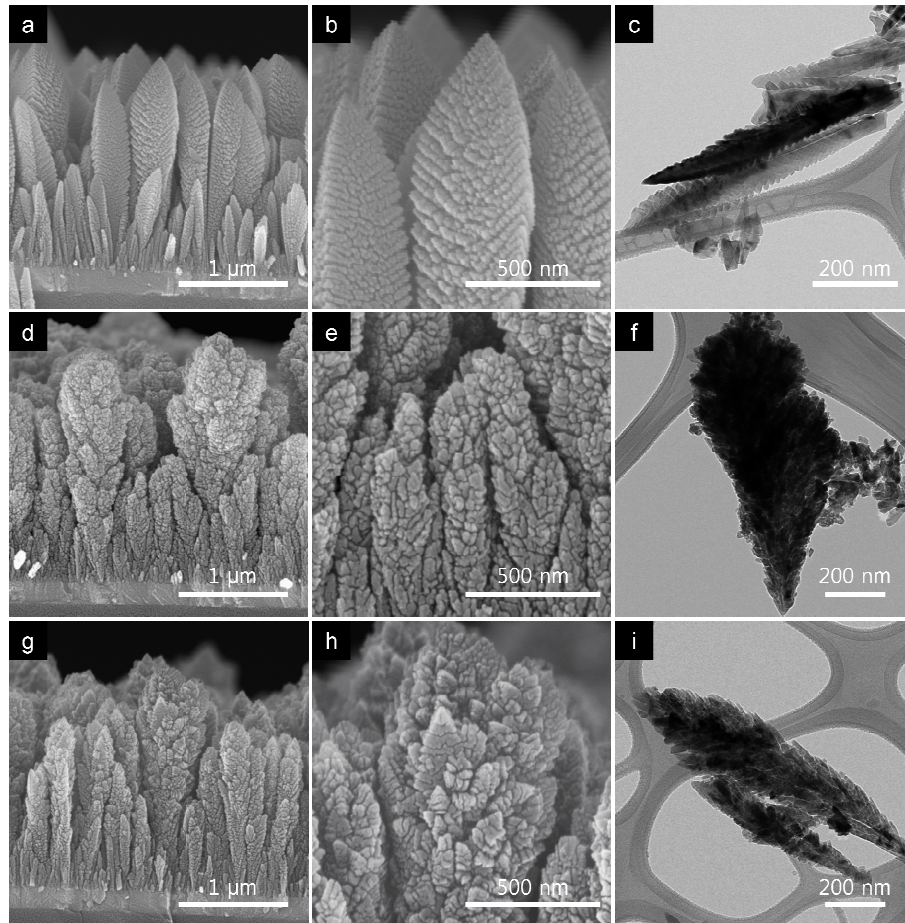
Figure 2.4. SEM and TEM images of (a), (b), (c) columnar, (d), (e), (f) granular and (g), (h), (i) branched TiO$_2$ films.

XRD patterns of as-prepared TiO$_2$ films are shown in Fig. 2.5. For all morphologies, the anatase phase of TiO$_2$ was synthesized. The XRD pattern of the columnar TiO$_2$ film shows a peak only for [112] direction of the anatase phase. This indicates that columns of the film were grown only in the preferred direction of [112]. On the other hand, the XRD pattern of the granular film is well matched with the particle diffraction file (PDF) reference peak of the anatase phase. This implies that small grains, composing the granular structure, were randomly deposited and not well oriented. The XRD pattern of the branched TiO$_2$ film is also closely matches the peaks from the PDF of anatase. However, the relative intensity of the peak of [101] direction was lower than that of the

granular structure. This could be because [101] direction from small primary particles initially deposited on the film was lost by sintering among them when forming branches.
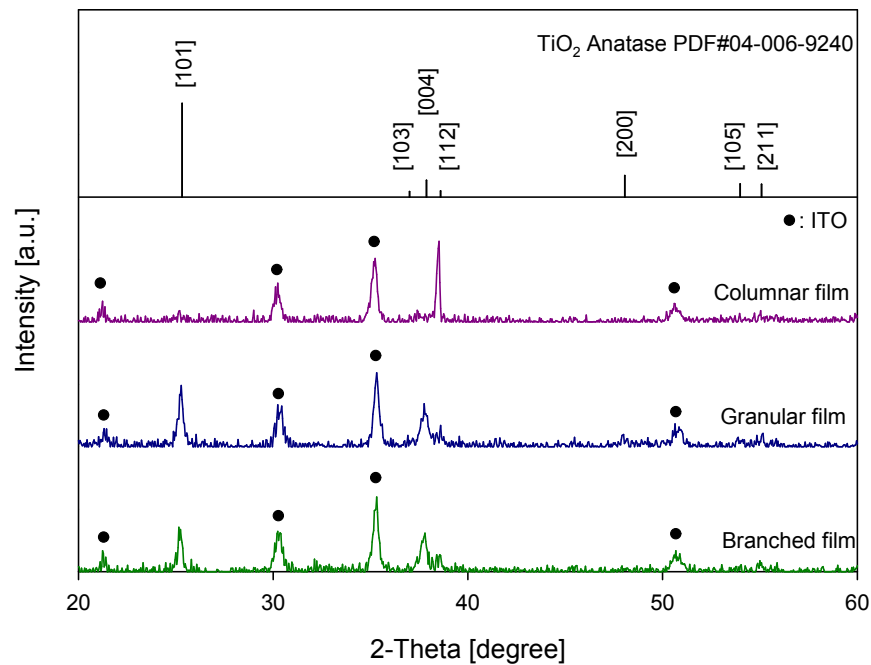
Figure 2.5. XRD patterns of columnar, granular, and branched TiO$_2$ films synthesized by ACVD. Black solid circles indicate peaks from Tin-doped Indium oxide (ITO) substrate.

UV-Vis absorption spectra of the TiO$_2$ films are shown in Fig. 2.6. In all films, the bandgap energy of TiO$_2$ was determined to be about 3.2 eV, which matches the reference bandgap energy of anantase TiO$_2$. This result means that all as-prepared films can be activated by light at wavelengths below 390 nm.
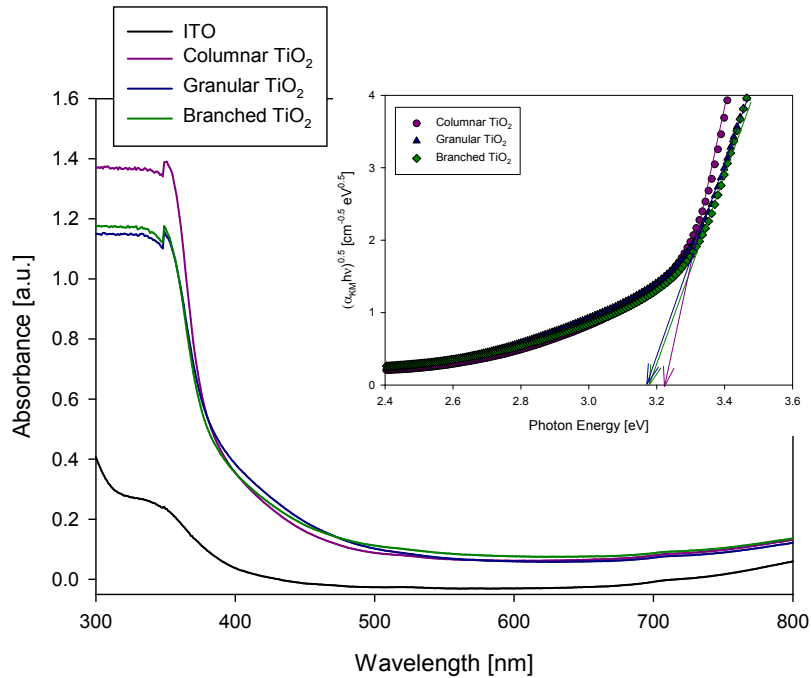
Figure 2.6. UV-Vis absorption spectra of as-prepared TiO$_2$ films and a correlation plot between photon energy and (α_{KM}hν)$^{0.5}$ to determine bandgap energy of the films (inset).

In Fig 2.7, measurement of light intensity of the arc Xe lamp shows that the blue band pass filter cut off UVB and UVC. Although both UVB and UVC were completely removed with the filter, the filtered light still includes UVA which can activate TiO$_2$ films.

Figure 2.8 shows the effect of irradiation light on the viability of *E. coli* with and without the blue band pass filter. While 10% of *E. coli* was inactivated after 2 h of irradiation with the filter in place, 99.999% of *E. coli* was killed within 30 min by irradiation of light without the filter. This result implies that UVB and UVC is lethal to *E. coli* cells whereas the effect of UVA is rather minimal over a period of two hours. Therefore, the blue band pass filter was attached to the lamp to minimize the effect of UV light on the inactivation of *E. coli* cells when examining inactivation efficiency by photochemical and photoelectrochemical reactions. In addition it was confirmed that TiO$_2$ itself does not

have any effect on the inactivation of *E. coli* with and without external voltage in dark conditions. (Fig. 2.9)
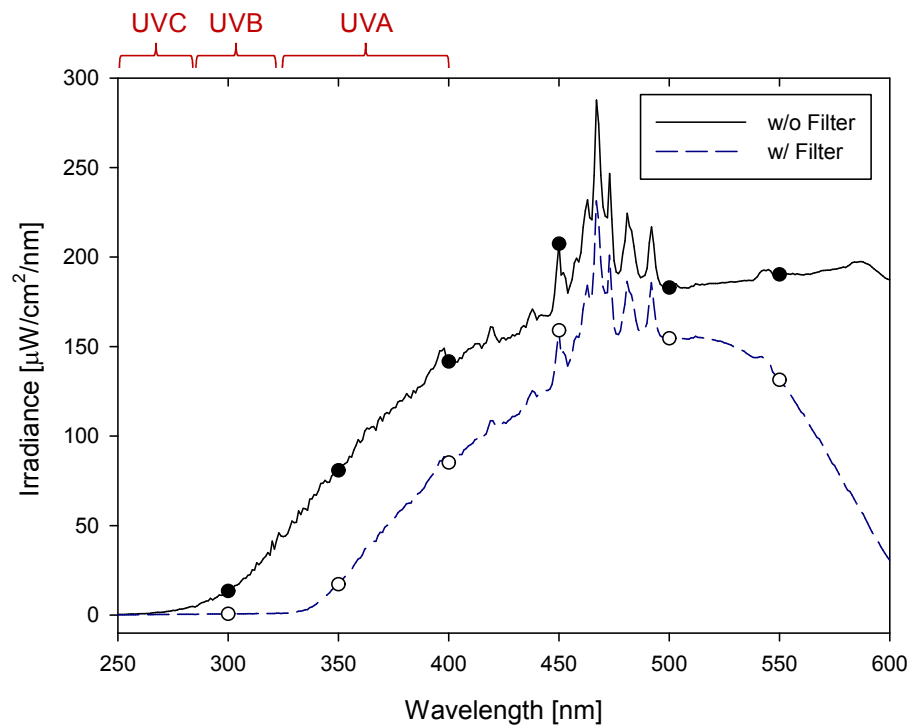
Figure 2.7. Light intensity of the arc Xe lamp operated by a 450 W power supply with and without a blue band pass filter.
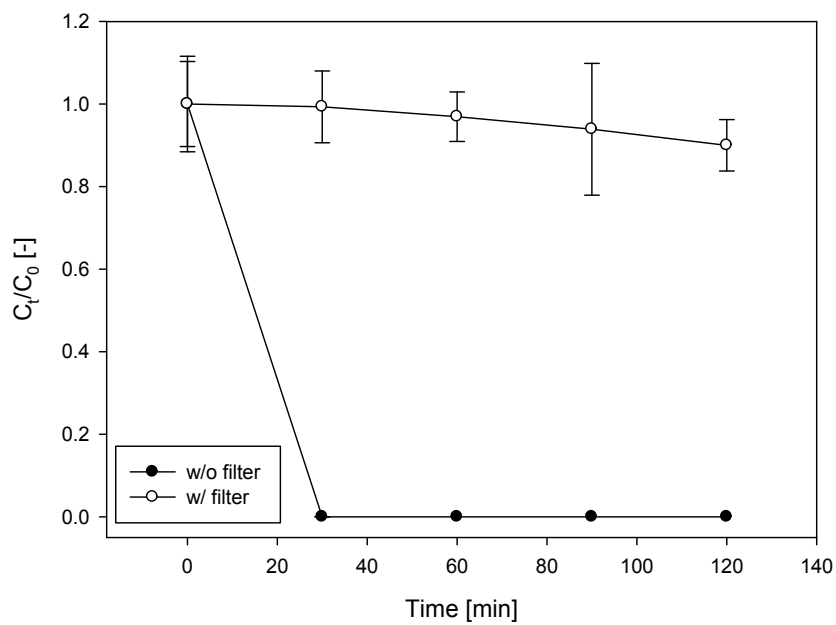
Figure 2.8. Effect of light only on *E. coli* viability with and without the blue pass filter.
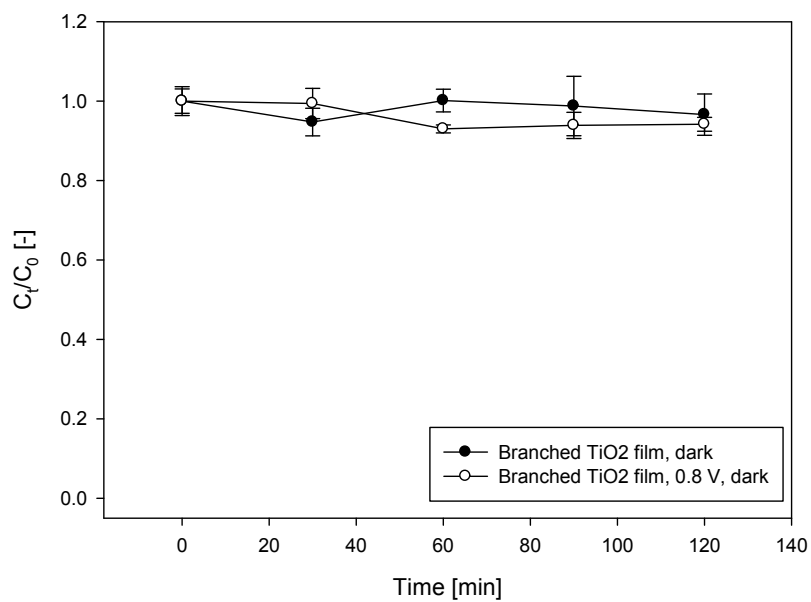
Figure 2.9. Effect of TiO$_2$ film on *E. coli* viability with and without external voltage in the dark.

Results of photochemical and photoeletrochemical inactivation of *E. coli* using a columnar, granular and a branched TiO_2 films are shown in Fig. 2.10. In all cases, concentration of *E. coli* seems to exponentially decrease with respect to inactivation time. This indicates that inactivation of *E. coli* follows Chick's Law which says that inactivation rate of bacteria can be expressed as a first ordered reaction with respect to concentration of viable cells in a reactor.[64] According to the Chick's Law inactivation rate can be given as follows:

$$Rate = \frac{dC_t}{dt} = -kC_t \quad (2.2)$$

where C_t is active cell concentration at time t. From Equation (2) inactivation rate constant, k can be obtained as Equation (2.3).

$$k = -\frac{\ln \frac{C_t}{C_0}}{t} \quad (2.3)$$

When inactivation rate is normalized by surface area of the films, normalized rate can be obtained as follow:

$$NormalizedRate = \frac{1}{A}\frac{dC_t}{dt} = -k'C_t \quad (2.4)$$

where A is surface area of the films and k' is normalized rate constant.

$$k' = \frac{k}{A} \quad (2.5)$$
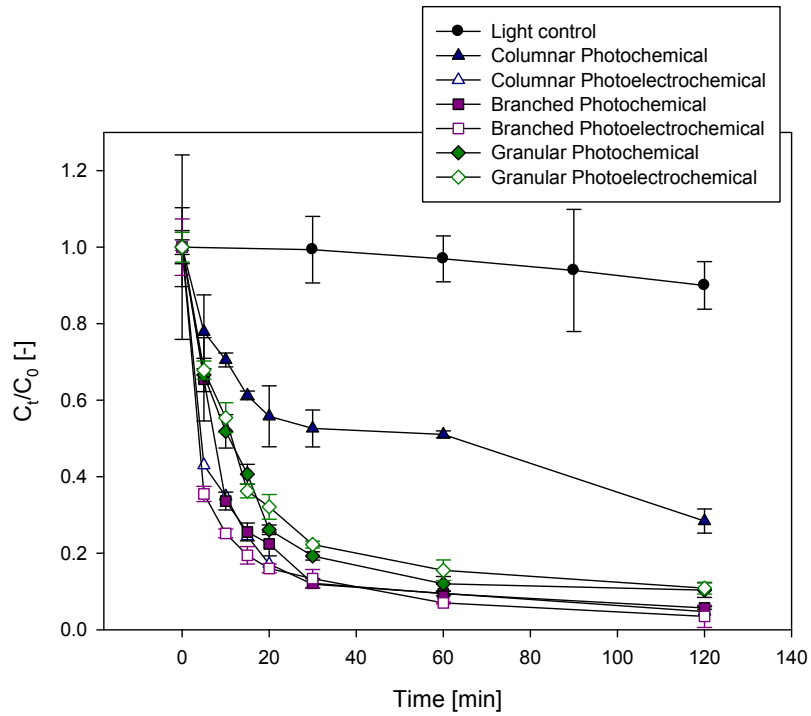
Figure 2.10. Photochemical and photoelectrochemical inactivation of *E. coli* using columnar, granular, and branched TiO$_2$ films.
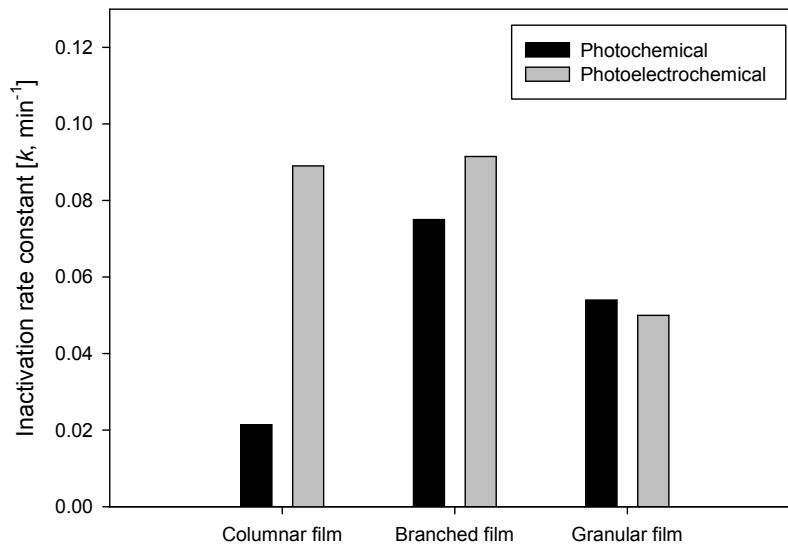
Figure 2.11. Inactivation rate constant of photochemical and photoelectrochemical inactivation of *E. coli* using columnar, granular, and branched TiO$_2$ films.
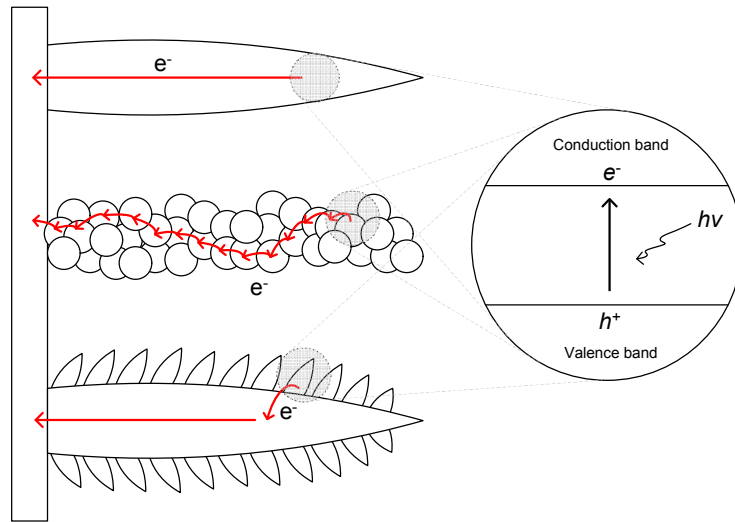
Figure 2.12. Electron transfer through a columnar, a granular and a branched TiO$_2$ film.

Since initial concentration C$_0$ was fixed as 10^8 cells/mL, the inactivation rate constant can represent the inactivation efficiency by photochemical and photoelectrochemical reaction for each kind of film. The k value for each case was obtained from the linear slope of a log scale plot of photochemical and photoelectrochemical inactivation of *E. coli*. The inactivation rate constant, k for each case is shown in Fig. 2.11. In the case of inactivation using the columnar TiO$_2$ film, the rate constant of photoelectrochemical inactivation was 430% higher than that of photochemical inactivation. This could be caused by a reduced electron-hole recombination rate due to enhancement of electron transfer to the cathode (platinum wire) through the column which does not have any grain boundary effect. (Fig. 2.12) Thus, more electron-hole pairs could generate more reactive oxygen species, which could result in a higher inactivation rate of *E. coli*. On the other hand, the photoelectrochemical reaction rate constant by the branched TiO$_2$ film was only 130% higher than photochemical reaction rate constant. Although an applied voltage (0.8 V) between the anode (TiO$_2$ film) and the cathode (platinum wire) was able to promote separation of electron-hole pairs generated in the TiO$_2$, grain boundaries between branches and main column could interrupt the fast transfer of electrons, consequently limiting the overall enhancement of the rate constant (Fig. 2.12). This phenomenon was significantly shown in the case of the granular film. In this case, the

photochemical and the photoelectrochemical rate constants were almost same, which means that electric bias could not enhance e-h separation in the film.

Table 2.3. Estimated Surface Area of TiO$_2$ Films

	Columnar film	Granular film-1	Granular film-2	Branched film
Total surface area of TiO$_2$ (m^2)	6.88×10^{-4}	3.18×10^{-3}	1.69×10^{-2}	6.34×10^{-3}
Normalized rate constant of PC[a] by surface area (k', min^{-1} m^{-2})	31.1	16.9	3.2	11.8
Normalized rate constant of PEC[b] by surface area (k', min^{-1} m^{-2})	129.4	15.7	2.9	14.4

[a] Photochemical inactivation. [b] Photoelectrochemical inactivation.

Surface area of the films could also significantly affect the inactivation rate. Larger surface area of TiO$_2$ can promote release of electrons and holes from the TiO$_2$ film into the buffer solution generating reactive oxygen species. Eventually this is able to enhance inactivation rate. The photochemical reaction rate constants reported in Fig. 2.11 for three different morphologies exhibit this surface area effect. No separation of electron-hole pairs by an applied electric potential occurred in the case of photochemical inactivation, therefore the rate constants could be affected by surface area of the films. As shown in Fig. 2.11 the photochemical inactivation rate constants of the branched and the granular TiO$_2$ film were 380% and 260% higher respectively than that of the columnar film. These larger inactivation rate contants reflect the fact the branched film

41

and the granular film (case of Granular film-1 in Table 2.3) has a 920% and 460% larger surface area than the columnar film (Table 2.3).
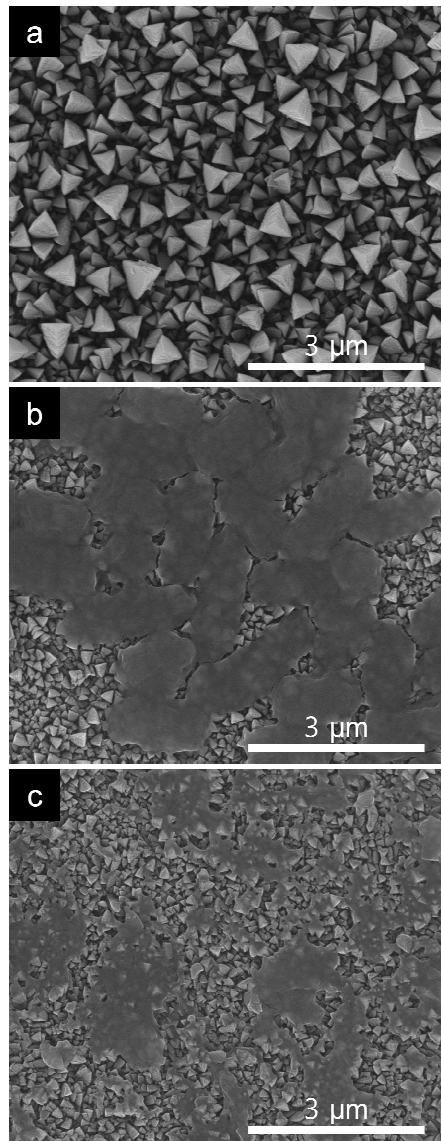
Figure 2.13. SEM images (top view) of columnar TiO$_2$ film (a) before and (b), (c) after inactivation.

Sunanda et al. well established a mechanism for inacitivation of *E. coli* cells by reactive oxygen species that are generated by a photocatalyst. The reactive species such as

hydroxyl radicals can oxidize and eventually destruct lipids in bacterial membrane. After destruction of cell membrane ions, protein and RNA are rapidly released out and this causes cell death.[56] SEM images after inactivation is well supporting this mechanism. Figure 2.13 (b) shows that *E. coli* cells were attached on the surface of the TiO_2 film after inactivation. It is clearly shown that surface of the cells is deforming. In Fig. 2.13 (c), cells were completely destructed.
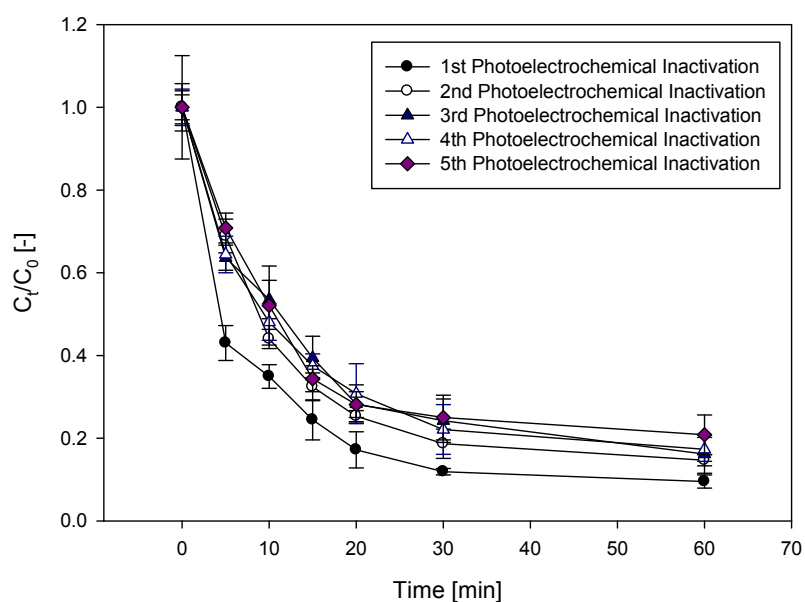
Figure 2.14. Photoelectrochemical inactivation of *E. coli* in series using a columnar TiO_2 films.
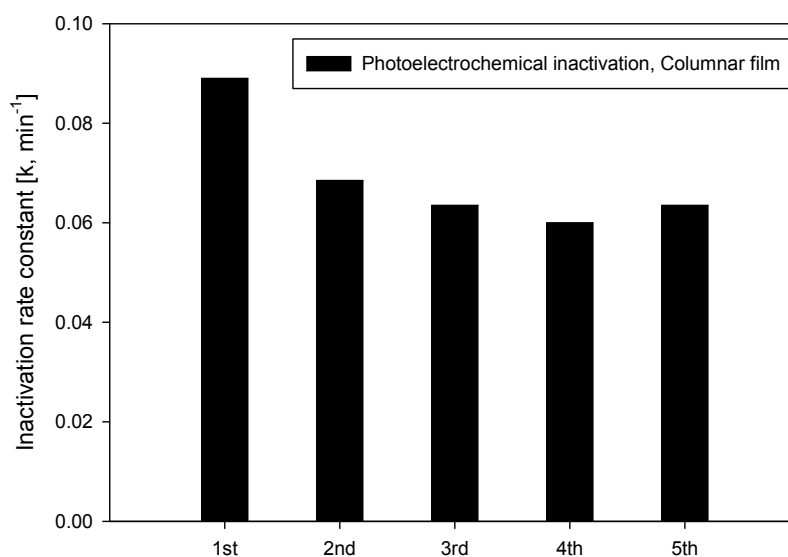
Figure 2.15. Change of photoelectrochemical inactivation rate constant with respect to repeated inactivations.

Figures 2.14 and 2.15 show change of inactivation rate with respect to number of times in case of repeated inactivation. As shown in Fig. 2.15 inactivation rate decreased about 22% at the second inactivation compared to the first one. And then it was maintained similarly. The first drop of the inactivation rate could occur due to inactivated cells attached on the film surface as shown in Fig. 2.13. These residual cells could block activation site of the TiO_2 film. Because these cells are completely decomposed finally, inactivation rate could be sustained after the second inactivation. The results also show that the TiO_2 film is sustainable material for the photocatalytic inactivation of *E. coli* in water.

2.4   Conclusions

TiO_2 films having different morphology: columnar, granular and branched structures were successfully synthesized via ACVD method to inactivate *E. coli* in water. In all

conditions thickness was well controlled at about 2 μm and anatase phase films were obtained. 99.999% of *E. coli* was rapidly killed within 30 min by irradiation of UVB and UVC in the absence of the TiO_2 films. However, 10% of *E. coli* was inactivated by irradiating UVA within 2 h. The TiO_2 films did not have any bactericidal effects on *E. coli* in the dark condition whereas they inactivate *E. coli* cells in water by the photochemical and the photoelectrochemical reaction with 1st order reaction rate under irradiation of UVA light. In case of the columnar TiO_2 film, the photoelectrochemical inactivation rate was 430% higher than the photochemical inactivation rate. On the other hand, only 130% increased on inactivation rate by the applied voltage in case of the branched TiO_2 film. In case of the granular film, both inactivation rates were similar. This significant difference on different morphologies indicates that inactivation rate could be enhanced more in the columnar structure than in the branched or even the granular one by the applied voltage. It could be caused by different electron transfer rate through the TiO_2 films, which affects recombination rate of e-h pairs generated by photoactivation. Total surface area of TiO_2 films for each morphology was estimated. The branched and the granular structure would have 9 times and 2.5 times larger surface area than the columnar structure repectively. The much larger surface area caused much faster inactivation of *E. coli* in the photochemical reaction. The TiO_2 film showed sustained inactivation rate for repeated inactivation although the second inactivation rate slightly reduced compared to the first inactivation.

Appendix A

Photocatalytic Pathways For CO$_2$ Reduction

Step 1: Photoexcitation (*e-h* Generation/Recombination)

Photocatalyst + $hv \rightarrow$ e$^-$ + h$^+$ (1)

e$^-$ + h$^+$ $\rightarrow$ heat   (2)
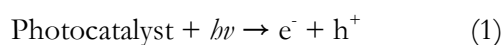
Step 2: CO$_2$ Reduction Pathways

As explained before, to reduce CO$_2$, the semiconductor is required to have its conduction band electrons with higher energy compared to the CO$_2$ reduction potential while the holes in the valence band to be able to oxidize water to O$_2$.

Valence Band (Photooxidation)

2H$_2$O + 4h$^+$ $\rightarrow$ O$_2$ + 4H$^+$ (3)

Conduction Band (Photoreduction)

Most of the researchers agree that the CO$_2$ photoreduction process is multi-electron transfer instead of single electron transfer as the electrochemical potential of -2.0 V for a single electron process does not support it.[36] The possible reactions that can occur in the reduction of CO$_2$ in aqueous medium with multi-electron transfer are shown as follows.
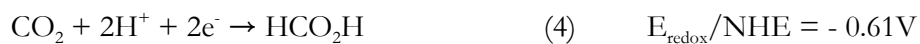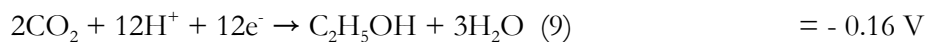
CO$_2$ + 2H$^+$ + 2e$^-$ $\rightarrow$ HCO$_2$H   (4) E_{redox}/NHE = - 0.61V

CO$_2$ + 4H$^+$ + 4e$^-$ $\rightarrow$ CH$_2$O + H$_2$O   (5)   = - 0.52 V

$$CO_2 + 2H^+ + 2e^- \rightarrow CO + H_2O \qquad (6) \qquad = -0.48V$$

$$CO_2 + 6H^+ + 6e^- \rightarrow CH_3OH + H_2O \qquad (7) \qquad = -0.38 \text{ V}$$

$$CO_2 + 8H^+ + 8e^- \rightarrow CH^4 + 2H^2O \qquad (8) \qquad = -0.24 \text{ V}$$

$$2CO_2 + 12H^+ + 12e^- \rightarrow C_2H_5OH + 3H_2O \quad (9) \qquad = -0.16 \text{ V}$$

Although the formation of methane, methanol and ethanol is thermodynamically favorable, it requires more electrons and protons. These products are more likely produced in CO_2 photoreduction in aqueous solutions, since more protons can be produced by water.[12,18]

Appendix B

Summary of Chemical and Biological Approach for CO_2 Reduction

Table B. 1. Photocatalytic Reduction of CO_2

Catalyst	Morphology /Properties	Reductants	Light Source	Products and Conversation rate	Synthesis Methods	References
TiO_2 (P25)	Powder, 24 nm	Isopropyl alcohol	4.2 kW, Xe lamp	CH_4 (1.2 μmol/g) HCO_2H	As purchased	Kaneco et al, *J. Photochem Photobiol. A.* 1998, 115, 223
$Cu-TiO_2$	Powder, 20 nm Anatase	Water, NaOH	Hg Lamp 254 nm, 364 nm	Methanol (700 μmol/g)	Sol-gel	Tseng et al, *J. Catal.,* 2004, 221, 432
$MWCNT-TiO_2$	Nanotubes, Anatase/ Rutile	Water	15W UV Lamp, 365 nm	CH_4 (73.33), HCO_2H (93.35), C_2H_5OH (149.36 μmol/g)	Sol-gel, Thermal hydrolysis	Xia et al, *Carbon,* 2007, 45, 717
Pt/Cu- N doped TiO_2	Nanotubes	Water	Solar	H_2 (200 ppm/cm²/h)	Anodic oxidation followed by metal sputtering	Varghese et al., *Nano Lett.,* 2009, 9, 731
$Ag-TiO_2$; $Cu-Fe-TiO_2$-SiO_2	Particles coated on fiber	Water	UV 365nm 10W/cm², Solar	Methanol (4.12 μmol/g/h), Methane, Ethylene	Thermal hydrolysis	Wu et al., *Catal Surv. Asia,* 2009, 13, 30
Ti-β-zeolite	Mesoporous	Water vapor	Hg lamp 100W, 250nm	CH_4 (24 μmol/g/h),	Thermal hydrolysis	Ikeue et al. *J. Phys. Chem. B,* 2001, 105, 8350
TiO_2 modified by enzyme and	Powder nanoparticles	MES	Tungsten, Halogen	CO (250 μmol/g-	Modified P25	Woolerton et al. *J. Am. Chem.*

photosentinizer			lamp 45 mW/cm^2	TiO_2/h)	(25nm)	*Soc.* 2010 ASAP
$CdSe/Pt/TiO_2$	Nanoparticles deposited on glass slide in the reaction cell	Water	300 W Xe lamp (>420nm) 100 mW/cm^2	CH_4 (48 ppm /g/h), CH_3OH 3.3 , CO and H_2	Impregnation (Pt-TiO_2) Mixing w/CdSe	Wang et al. *J. Phys. Chem. Lett.* 2010, 1, 48
$Cu-TiO_2/SiO_2$	Mesoporous	Water	450 W Xe lamp	CO (60 µmol/g-TiO_2/h) CH_4 (10 µmol/g-TiO_2/h)	Sol-gel	Li et al., 2010
$Cu-TiO_2/SiO_2$	Mesoporous	Water	450 W Xe lamp	CO (25 µmol/g-TiO_2/h)	FuAR	Wang et al., 2011 (The thesis Chap. 1)
TiO_2	Columnar film	Water	450 W Xe lamp	CO (239 µmol/g-TiO_2/h)	ACVD	In preparation
$Pt-TiO_2$	Columnar film	Water	450 W Xe lamp	CO (180 µmol/g-TiO_2/h) CH_4 (1361 µmol/g-TiO_2/h)	ACVD Sputtering	In preparation

Table B. 2. CO$_2$ Capture by Algae

Microorganism	Feed gas	Culture density and form of existence	Light source	Products and capture rate	Reference
Chlorella kessleri	18% CO2 T=313 K	N/A	N/A	CO$_2$ (0.163 g/L/day) =154μmol/L /h	Morais et al., Energy *Conversion and Management*, 2007,48, 2169
Chlorococcum littorale	40 % CO2 T=323K	chlophyll (Chl) in both algae ranged from 6 to 8 μg/ml	1000 μEn /cm²/s, filtered through a cut-off filter (>620 nm) and a 3 cm layer of water	CO$_2$ (1 g/L/day) =947μmol/L /h	Iwasaki, et al. *J. Photochem. Photobiol. B*, 1998, 44, 184
Chlorella vulgaris	15 % CO2 T=300K	Algae 0.04 g dry weight per litter in artificial wastewater	White light 110 μEn /m²/s	CO$_2$ (591μmol/L/ h NH$_3$(54.7μmo l/L/h)	Yun et al., *J. Chem. Tech. Biotechnol.*, 1997, 69, 451

References

1.   M. Halmann and M. Steinberg, *Greenhous Gas Carbon Dioxide Mitigation: Science and Technology*, Lewis Publishers, Boca Raton, FL, 2000.

2.   P. Usubharatana, D. McMartin, A. Veawab and P. Tontiwachwuthikul, *Industrial & Engineering Chemistry Research*, 2006, **45**, 2558-2568.

3.   B. Metz, O. Davidson, H. de Coninck, M. Loos and C. Meyer, New York, 2005.

4.   C. S. Song, *Catalysis Today*, 2006, **115**, 2-32.

5.   M. Kitano, M. Matsuoka, M. Ueshima and M. Anpo, *Applied Catalysis a-General*, 2007, **325**, 1-14.

6.   V. P. Indrakanti, J. D. Kubicki and H. H. Schobert, *Energy & Environmental Science*, 2009, **2**, 745-758.

7.   M. Anpo, H. Yamashita, Y. Ichihashi, Y. Fujii and M. Honda, *Journal of Physical Chemistry B*, 1997, **101**, 2632-2636.

8.   M. Anpo, H. Yamashita, K. Ikeue, Y. Fujii, S. G. Zhang, Y. Ichihashi, D. R. Park, Y. Suzuki, K. Koyano and T. Tatsumi, *Catalysis Today*, 1998, **44**, 327-332.

9.   H. Yamashita, M. Honda, M. Harada, Y. Ichihashi, M. Anpo, T. Hirao, N. Itoh and N. Iwamoto, *Journal of Physical Chemistry B*, 1998, **102**, 10707-10711.

10.   K. Ikeue, H. Yamashita, M. Anpo and T. Takewaki, *Journal of Physical Chemistry B*, 2001, **105**, 8350-8355.

11.   M. Ogawa, K. Ikeue and M. Anpo, *Chem Mater*, 2001, **13**, 2900-2904.

12.   I. H. Tseng, W. C. Chang and J. C. S. Wu, *Applied Catalysis B-Environmental*, 2002, **37**, 37-48.

13.   T. V. Nguyen and J. C. S. Wu, *Solar Energy Materials and Solar Cells*, 2008, **92**, 864-872.

14.   M. Anpo, S. G. Zhang, H. Mishima, M. Matsuoka and H. Yamashita, *Catalysis Today*, 1997, **39**, 159-168.

15.   H. Yamashita, Y. Fujii, Y. Ichihashi, S. G. Zhang, K. Ikeue, D. R. Park, K. Koyano, T. Tatsumi and M. Anpo, *Catalysis Today*, 1998, **45**, 221-227.

16. Y. J. Xu, T. F. Xie, D. J. Wang, Y. Wang and T. J. Li, *Chemical Journal of Chinese Universities-Chinese*, 1999, **20**, 461-463.

17. W. Y. Lin, H. X. Han and H. Frei, *Journal of Physical Chemistry B*, 2004, **108**, 18269-18273.

18. X. H. Xia, Z. H. Jia, Y. Yu, Y. Liang, Z. Wang and L. L. Ma, *Carbon*, 2007, **45**, 717-721.

19. Y. Li, W. N. Wang, Z. L. Zhan, M. H. Woo, C. Y. Wu and P. Biswas, *Applied Catalysis B: Environmental*, 2011, **100**, 386-392.

20. S. Basak, K. S. Rane and P. Biswas, *Chem Mater*, 2008, **20**, 4906-4914.

21. W. N. Wang, W. Widiyastuti, T. Ogi, I. W. Lenggoro and K. Okuyama, *Chem Mater*, 2007, **19**, 1723-1730.

22. W. N. Wang, F. Iskandar, K. Okuyama and Y. Shinomiya, *Adv Mater*, 2008, **20**, 3422-3426.

23. W. N. Wang, Y. Kaihatsu, F. Iskandar and K. Okuyama, *Chem Mater*, 2009, **21**, 4685-4691.

24. F. Iskandar, L. Gradon and K. Okuyama, *J Colloid Interf Sci*, 2003, **265**, 296-303.

25. D. Sen, S. Mazumder, J. S. Melo, A. Khan, S. Bhattyacharya and S. F. D'Souza, *Langmuir*, 2009, **25**, 6690-6695.

26. S. T. Chang and O. D. Velev, *Langmuir*, 2006, **22**, 1459-1468.

27. R. B. Bird, W. E. Stewart and E. N. Lightfoot, *Transport Phenomena*, John Wiley & Sons, Inc., New York, 2002.

28. T. T. Kodas and M. Hampden-Smith, *Aerosol Processing of Materials*, Wiley-VCH, New York, 1999.

29. S. Lowell, J. E. Shields, M. A. Thomas and M. Thommes, *Characterization of Porous Solids and Powders: Surface Area, Pore Size and Density*, Springer, Dordrecht, The Netherlands, 2006.

30. O. D. Velev, A. M. Lenhoff and E. W. Kaler, *Science*, 2000, **287**, 2240-2243.

31. W. N. Wang, W. Widiyastuti, I. W. Lenggoro, T. O. Kim and K. Okuyama, *J Electrochem Soc*, 2007, **154**, J121-J128.

32. W. Widiyastuti, S. Y. Lee, F. Iskandar and K. Okuyama, *Adv Powder Technol*, 2009, **20**, 318-326.

33. F. Iskandar, H. W. Chang and K. Okuyama, *Adv Powder Technol*, 2003, **14**, 349-367.

34. S. P. Fisenko, W. N. Wang, I. W. Lenggoro and K. Okyuama, *Chem Eng Sci*, 2006, **61**, 6029-6034.

35. J. J. Hegseth, N. Rashidnia and A. Chai, *Phys Rev E*, 1996, **54**, 1640-1644.

36. A. J. Morris, G. J. Meyer and E. Fujita, *Accounts Chem Res*, 2009, **42**, 1983-1994.

37. A. H. Yahaya, M. A. Gondal and A. Hameed, *Chemical Physics Letters*, 2004, **400**, 206-212.

38. T. W. Woolerton, S. Sheard, E. Reisner, E. Pierce, S. W. Ragsdale and F. A. Armstrong, *Journal of the American Chemical Society*, 2010, **132**, 2132-2133.

39. S. K. Friedlander, *Smoke, Dust, and Haze: Fundamental of Aerosol Dynamics*, Oxford University Press, New York, 2000.

40. W. N. Wang, A. Purwanto, I. W. Lenggoro, K. Okuyama, H. Chang and H. D. Jang, *Industrial & Engineering Chemistry Research*, 2008, **47**, 1650-1659.

41. M. A. Shannon, P. W. Bohn, M. Elimelech, J. G. Georgiadis, B. J. Marinas and A. M. Mayers, Nature, 2008, 452, 301.

42. M. A. Montgomery and M. Elimelech, Environmental Science and Technology, 2007, 41, 17.

43. K. E. Kemper, Hydrogeology Journal, 2007, 12, 3

44. U. Szewzyk, R. Szewzyk, W. Manz and K. H. Schleifer, Annual Review of Microbiology, 2000, 54, 81.

45. K. Gopal, S. S. Tripathy, J. L. Bersillon and S. P. Dubey, Journal of Hazardous Materials, 2007, 140, 1.

46. S. W. Krasner, H. S. Weinberg, S. D. Richardson, S. J. Pastor, R. Chinn, M. J. Sclimenti, G. D. Onstad and A. D. Thruston, Environmental Science and Technology, 2006, 40, 7175.

47. D. Zhang, G. Li and J. C. Yu, Journal of Materials Chemistry, 2010, 20, 4529.

48. T. Matsunaga, R. Tomoda, T. Nakajima and H. Wake, FEMS Microbiology Letters, 1985, 29, 211.

49. C. Wei, W. -Y. Lin, Z. Zaina, N. E. Williams, K. Zhu, A. P. Kruzic, R. L. Smith and K. Rajeshwar, Environmental Science and Technology, 1994, 28, 934.

50. C. Hu, Y. Lan, J. Qu, X. Hu and A. Wang, Journal of Physical Chemistry B, 2006, 110, 4066.

51. C. Hu, J. Guo, J. Qu and X. Hu, Langmuir, 2007, 23, 4982.

52. P. Wang, B. Huang, X. Qin, X. Zhang, Y. Dai and M. -H. Whangbo, Inorganic Chemistry, 2009, 48, 10697.

53. C. Mccullagh, J. M. C. Robertson, D. W. Bahnemann and P. K. J. Robertson, Research on Chemical Intermediates, 2007, 33, 359.

54. P. Amezaga-Madrid, G. V. Nevarez-Moorillon, E. Orrantia-Borunda, M. Miki-Yoshida, FEMS Microbiology Letters, 2002, 211, 183.

55. K. P. Kuhn, I. F. Chaberny, K. Massholder, M. Stickler, V. W. Benz, H. -G. Sonntag, L. Erdinger, Chemosphere, 2003, 53, 71.

56. K. Sunada, T. Watanabe, K. Hashimoto, Journal of Photochemistry and Photobiology A, 2003, 156, 227.

57. M. P. Reddy, H. H. Phil, M. Subrahmanyam, Catalysis Letters, 2008, 123, 56.

58. H. Yu, X. Quan, Y. Zhang, N. Ma, S. Chen and H. Zhao, Langmuir 2008, 24, 7599.

59. S. C. Hayden, N. K. Allam and M. A. El-Sayed, Journal of the American Chemical Society, 2010, 132, 14406.

60. E. Thimsen, N. Rastgar and P. Biswas, Journal of Physical Chemistry C, 2008, 112, 4134.

61. W. -J. An, E. Thimsen and P. Biswas, Journal of Physical Chemistry Letters, 2010, 1, 249.

62. W. -J. An, D. D. Jiang, J. R. Matthews, N. F. Borrelli and P. Biswas, Journal of Materials Chemistry, 2011, 21, 7913.

63. D. Reyes-Coronado, G. Rodriguez-Gattorno, M. E. Espinosa-Pesqueira, C. Cab, R. Coss and G. Oskam, Nanotechnology, 2008, 19, 145605.

64. J. C. Chang, S. F. Ossoff, D. C. Lobe, M. H. Dorfman, C. M. Dumais, R. G. Qualls and J. D. Johnson, Applied and Environmental Microbiology, 1985, 49, 1361.

Vita

Jinho Park

Date of Birth	**September 17, 1980**
Place of Birth	**Daejeon, South Korea**
Degrees	**B.S. Chemical Engineering, February 2006** **M.S. Chemical and Biomolecular Engineering, February 2008**

Publications

J. Park, E. M. Kettleson, W. J. An, Y. Tang, and P. Biswas* (2011) "Inactivation of *E. coli* in Water using Photocatalytic, Nanostructured Films Synthesized by Aerosol Routes", in preparation.

M. Sahu, J. Park, and P. Biswas* (2011) "*In-Situ* Charge Characterization of TiO$_2$ and Cu-doped TiO$_2$ Nanoparticles in a Flame Aerosol Reactor", *Journal of Nanoparticle Research*, submitted.

W. -N. Wang, J. Park, and P. Biswas* (2011) "Rapid synthesis of nanostructured Cu–TiO$_2$–SiO$_2$ composites for CO$_2$ photoreduction by evaporation driven self-assembly", *Catalysis Science and Technology*, 1, 593-600. (Selected as inside cover)

B. Lim, T. Yu, J. Park, Y. Zheng, and Y. Xia* (2011) "Mixing an Aqueous Suspension of Pd or Au Nanocrystals with a Less Polar Solvent Can Cause Changes to Size, Morphology, or Both", *Angewandte Chemie International Edition*, 50, 1-5.

K. Cho, H. Chang, D. S. Kil, J. Park, H. D. Jang*, and H. Y. Sohn (2009) "Mechanisms of the Formation of Silica Particles from Precursors with Different Volatilities by Flame Spray Pyrolysis", *Aerosol Science and Technology*, 43, 911-920.

K. Cho, H. Chang, J. Park, B. G. Kim, and H. D. Jang* (2008) "Effect of Molar Ratio of TiO$_2$/SiO$_2$ on the properties of particles synthesized by Flame Spray Pyrolysis", *Journal of Industrial and Engineering Chemistry*, 14(6), 860-863.

H. D. Jang*, H. Chang, K. Cho, S. J. Kim, <u>J. Park</u>, J. W. Choi, and K. Okuyama (2008) "Fabrication of porous nanostructured TiO$_2$ particles by an aerosol templating method", *Ultramicroscopy,* **108(10), 1241-1245.**

H. D. Jang*, H. Chang, H. S. Yoon, K. Cho, <u>J. Park</u>, and S. Y. Oh (2008) "Production of silica nanopowder from domestic siliceous mudstone", *Colloids and Surfaces A: Physicochemical and Engineering Aspects,* **313-314, 121-125.**

H. K. Chang, <u>J. Park</u>, and H. D. Jang* (2008) "Flame Synthesis of SiO$_2$ Nanoparticles by Adopting Two-Fluid Nozzle Spray", *Colloids and Surfaces A: Physicochemical and Engineering Aspects,* **313-314, 140-144.**

August 2011